


RESEARCH

Open Access



ALS-associated C21ORF2 variant disrupts DNA damage repair, mitochondrial metabolism, neuronal excitability and NEK1 levels in human motor neurons

Pavol Zelina^{1†}, Anna Aster de Ruyter^{1†}, Christy Kolsteeg¹, Ilona van Ginneken¹, Harmjan R. Vos³, Laura F. Supiot¹, Boudewijn M. T. Burgering³, Frank J. Meye¹, Jan H. Veldink², Leonard H. van den Berg² and R. Jeroen Pasterkamp^{1*} 

Abstract

Amyotrophic lateral sclerosis (ALS) is an adult-onset neurodegenerative disease leading to motor neuron loss. Currently mutations in >40 genes have been linked to ALS, but the contribution of many genes and genetic mutations to the ALS pathogenic process remains poorly understood. Therefore, we first performed comparative interactome analyses of five recently discovered ALS-associated proteins (C21ORF2, KIF5A, NEK1, TBK1, and TUBA4A) which highlighted many novel binding partners, and both unique and shared interactors. The analysis further identified C21ORF2 as a strongly connected protein. The role of C21ORF2 in neurons and in the nervous system, and of ALS-associated C21ORF2 variants is largely unknown. Therefore, we combined human iPSC-derived motor neurons with other models and different molecular cell biological approaches to characterize the potential pathogenic effects of C21ORF2 mutations in ALS. First, our data show C21ORF2 expression in ALS-relevant mouse and human neurons, such as spinal and cortical motor neurons. Further, the prominent ALS-associated variant C21ORF2-V58L caused increased apoptosis in mouse neurons and movement defects in zebrafish embryos. iPSC-derived motor neurons from C21ORF2-V58L-ALS patients, but not isogenic controls, show increased apoptosis, and changes in DNA damage response, mitochondria and neuronal excitability. In addition, C21ORF2-V58L induced post-transcriptional downregulation of NEK1, an ALS-associated protein implicated in apoptosis and DDR. In all, our study defines the pathogenic molecular and cellular effects of ALS-associated C21ORF2 mutations and implicates impaired post-transcriptional regulation of NEK1 downstream of mutant C21ORF2 in ALS.

Keywords Amyotrophic lateral sclerosis, Genetic mutation, Interactor, iPSC, Motor neuron

[†]Pavol Zelina and Anna Aster de Ruyter have contributed equally.

*Correspondence:

R. Jeroen Pasterkamp

r.j.pasterkamp@umcutrecht.nl

Full list of author information is available at the end of the article



Background

Amyotrophic lateral sclerosis (ALS) is a fatal adult-onset neurodegenerative disease characterized by the progressive loss of upper and lower motor neurons (MNs) resulting in muscle weakness and atrophy [1, 2]. The majority of ALS patients starts to develop symptoms between 51–66 years of age and median survival is 3–5 years after symptom onset [3]. Treatment options are limited with only a few FDA-approved drugs that have marginal effects on disease progression. The development of additional therapies requires a better understanding of the pathogenic mechanisms underlying ALS.

ALS is considered a “simplex” disease caused by a combination of genetic and environmental factors [4–6]. From a genetic point of view, 5–10% of patients are classified as having familial ALS (fALS), and the remaining 90–95% are sporadic ALS (sALS) patients [7, 8]. Currently, mutations in >40 genes have been reported to explain a large portion of fALS cases, and genetic defects have also been detected in approximately 10% of sALS cases [9, 10]. Although these genetic findings have helped defining ALS disease mechanisms [11–14], the contribution of many genes and genetic mutations to the ALS pathogenic process remains poorly understood.

To define the pathogenic mechanisms downstream of specific gene mutations, we have previously used proteomics techniques to identify protein binding partners of affected proteins [15, 16]. This work, for example, identified strongly overlapping interactomes for FUS (Fused in sarcoma)-ATXN2 (Ataxin-2)-TDP-43 (TAR DNA-binding protein 43) and for UBQLN2 (Ubiquilin 2)-OPTN (Optineurin), and discovered a role for fragile X mental retardation protein (FMRP) in FUS-ALS [16]. Here we expanded this approach and performed comparative interactome analysis of five additional proteins recently linked to ALS, i.e. Chromosome 21 open reading frame 2 (C21ORF2 also known as CFAP410) [17], Kinesin family member 5A (KIF5A) [18, 19], NIMA-related kinase 1 (NEK1) [20, 21], TANK-binding kinase 1 (TBK1) [22, 23], and Tubulin alpha 4A (TUBA4A) [24]. The most strongly connected protein in our dataset was C21ORF2 which was identified as a risk factor for ALS in a Genome Wide Association Study (GWAS) [17]. C21ORF2 is ubiquitously expressed and evolutionary conserved. It has been implicated in cytoskeletal regulation, DNA repair and primary cilia formation and stability [25–27]. Mutations in *C21ORF2* cause various ciliopathies, e.g. retinitis pigmentosa, cone-rod dystrophy [28], retinal dystrophy [29], Jeune syndrome [27, 30] and axial spondylometaphyseal dysplasia [31]. C21ORF2 binds NEK1, another ALS-associated protein, that regulate the DNA damage response (DDR). The function of C21ORF2 in the nervous system is unknown. It was first described in an exon trapping

study aimed at identifying genes responsible for Down syndrome and other hereditary disorders originating from chromosome 21, suggesting a role in brain development [32]. However, whether or how *C21ORF2* variants cause ALS-relevant phenotypes is unknown.

In this study, we performed interactome analyses of five more recently identified ALS-associated proteins (C21ORF2, KIF5A, NEK1, TBK1, and TUBA4A). These data will provide a valuable framework for further analysis of the pathogenic mechanisms and therapeutic potential of these different ALS-associated proteins. The interactome analysis identified C21ORF2 as a strongly connected protein and we therefore first performed expression studies to detect C21ORF2 expression in MNs and other ALS relevant neuron types. Based on these results, we expressed the prominent ALS-related variant C21ORF2-V58L [17] in zebrafish embryos, which caused motor deficits *in vivo*. To dissect these effects at the cellular level, we generated iPSCs, and corresponding isogenic controls, from patients carrying C21ORF2-V58L mutations. Subsequent analysis of iPSC-derived MNs revealed that C21ORF2-V58L causes increased apoptosis, decreased DDR, changes in mitochondria activity, altered electrophysiological properties, and decreased expression of NEK1 in human MNs *in vitro*. Interestingly, downregulation of NEK1 has been reported to lead to apoptosis and altered DDR [26, 33–37]. Together, these results define the pathogenic effects of C21ORF2-V58L mutations and suggest that mutant C21ORF2 may impair the post-transcriptional regulation of NEK1 to induce MN degeneration and defective motor behavior.

Methods

Animal use and care

All animal experiments in this study were approved by the Centrale Commissie Dierproeven of Utrecht University (CCD license: AVD 1150020171565) and were in accordance with Dutch law (Wet op de Dierproeven 2014) and European regulations (guideline 2010/63/EU). C57BL/6J mice obtained from Charles River Laboratories (Wilmington, Massachusetts, USA) were housed at 22 ± 1 °C on a wood-chip bedding supplemented with tissue on a 12 h/12 h day/night cycle. Animals were fed *ad libitum*.

Tissue collection, fixation and immunostaining

Mice were deeply anesthetized with Euthanial (Alfasan) and intracardially perfused with ice-cold phosphate buffered saline (PBS, pH 7.4) followed by 4% paraformaldehyde (PFA) (104,005,100, Merck) in PBS. Brain and spinal cord were dissected and fixed overnight (ON) in 4% PFA at 4 °C. Fixed tissue was cryoprotected in 10% sucrose for 24 h and then in 30% sucrose at 4 °C until

saturation. Tissue was snap-frozen in isopentane at -45°C and stored at -80°C . For brain and spinal cord tissue, $20\ \mu\text{m}$ sections were obtained using a Leica CM1950 cryostat and mounted on SuperFrost Plus slides (Thermo Fisher Scientific). For immunofluorescent staining, brain and spinal cord tissue sections were blocked in PBSGT ($1\times\text{PBS}+0.2\%$ gelatin (Merck, cat#48,723) $+0.5\%$ Triton X-100) for 1 h at room temperature (RT). Primary antibodies were incubated ON at 4°C in PBSGT. Alexa Fluor-conjugated secondary antibodies (1:500) were diluted in PBSGT and slides were incubated ON at 4°C . Primary antibodies used: anti-CTIP ab18465 abcam, anti-CHAT AF3447 R&D Systems, anti-C21ORF2 ab167351 abcam, anti-NEK1 A304-569A Bethyl Laboratories. 4,6-diamidino-2-phenylindole (DAPI) was used to stain nuclei. Slides with sections were washed $3\times 15\ \text{min}$ in 0.5% Triton-X-100 in PBS (PBS-T) after each antibody and DAPI incubation. All slides and coverslips were mounted with FluorSave™ Reagent (Millipore, Cat. No. 345789), left to dry at RT and stored at 4°C .

Mouse primary cortical neuron cultures

For plating neurons, 18 mm glass coverslips were placed in 12-well plates and coated with $20\ \mu\text{g}/\text{ml}$ poly-D-lysine (PDL)(P7888, Sigma) for 30 min at RT. PDL was subsequently removed, coverslips washed $3\times$ with $1\times\text{PBS}$, followed by the coating of the coverslips with $3.0\ \mu\text{g}/\text{ml}$ laminin (L2020-1MG, Sigma) for 1 h at 37°C . After incubation, excessive laminin was removed and 1 ml culture medium (Neurobasal medium (21,103–049, Gibco), B-27 (12,587, Gibco), L-glutamine (25,030,081, Gibco), pen-strep (15,140–122, Gibco), 20 mM glucose (16,301, Sigma-Aldrich) was added to the well. For this study C57BL/6 J female mice from The Jackson Laboratory (RRID: IMSR_JAX:000664) were used. Cervical dislocation was applied to sacrifice timed pregnant mice on E15.5 (day of plug was considered as embryonic day 0.5 (E0.5)). Embryos were collected in ice-cold PBS and both male and female embryos were used. The cortices of two embryos were dissected and brought into a sterile Eppendorf tube. Cortices in the Eppendorf tube were trypsinised by the addition of 1 ml fresh ice-cold PBS and $20\ \mu\text{l}$ of 0.05% trypsin and were incubated for 15 min at 37°C . Subsequently, supernatant was removed and 1 ml of dissociation medium (L15 medium (Thermo Fischer Scientific, cat# 21,083,027), 10% FBS, $10\ \mu\text{g}/\text{ml}$ DNase I (diluted 1:1000, VWR International, cat#A3778.0010)) was added and tissue was gently triturated until no pieces of tissue were visible using $200\ \mu\text{l}$ pipet. Next, cells were spun down with a small bench rotor for approximately 10 s, supernatant was removed and 1 ml of Opti-MEM was added to the cells. In a new Eppendorf tube, $10\ \mu\text{l}$ of the cell suspensions was diluted 1:100 in 1 ml Opti-MEM

to count the cells. The volume of the cell suspension containing 1,000,000 cells was pipetted into a third sterile Eppendorf tube. Once again, supernatant was removed after the Eppendorf tube was spun down using a small bench rotor. $100\ \mu\text{l}$ of Opti-MEM and $10\ \mu\text{g}$ of the specific DNA were added to the cells. The cells with the DNA were dissociated by repeatedly pipetting up and down. Subsequently, the cell suspension was transferred to electroporation cuvettes (EC-0002S, NEPA GENE). Electroporation was performed with a NEPA21 Type II electroporator. The settings used for electroporation remained the same for all experiments; poring pulse 175 V (duration: 5 ms; interval: 50 ms; number of pulses: 2; decay: 10%; one direction) and transfer pulse 20 V (duration: 50 ms; interval: 50 ms; number of pulses: 5; decay: 40%; two directions). Afterwards, 300,000 transfected cells were seeded on the prepared coverslips. The cortical neurons were maintained for 3–5 days in culture medium (1/2 changed every 48 h), following which cells were fixed and processed for future analyses.

For cCAS3 analyzes primary cortical neurons were stained for β 3-TUBULIN (TUJ1) to stain neurons and for cCAS3 to detect apoptotic neurons. Pictures were taken using a confocal microscope (Olympus FV1000) with a $20\times$ objective to visualize several neurons in one optical field. At least 8 neighboring optical fields covering more than 100 neurons were taken per experiment and condition. Percentages of GFP-positive neurons (expressing GFP or GFP-C21ORF2 variants) that are also positive of cCAS3 were quantified for each optical field and statistical differences between conditions were analyzed with GraphPadPrism.

C21orf2 variant constructs

Human *C21ORF2* DNA NM_001271441.1 (NP_001258370) was used to create deletion (Supplementary material 3: Supplementary Fig. S3A) and mutant variants (Supplementary material 14: Supplementary Table S5) of *C21ORF2* protein. Mutations of *C21ORF2* were created by PCR site-directed mutagenesis. *C21ORF2* constructs were cloned into the BamHI-HindIII sites of pEGFP-C1 (CLONTECH) for transfection into N2a cells. For expression in primary neurons, *EGFP-C21ORF2* constructs were digested out from pEGFP-C1 and ligated into of pCX-MCS-reverse (kind gift of Prof. Alain Chedotal, Vision Institute, Paris, France) using AgeI-MfeI sites. All expression plasmids were amplified in DH5 α bacteria (Thermo Fisher, 18,265,017).

Culture of N2a cells

N2a cells (ATCC, CCL-131) were maintained in T75 flasks (Greiner CELLSTAR) containing 10 ml growth medium (Dulbecco's Modified Eagle Medium (DMEM)

high glucose formulation (41,966–029, Gibco) supplemented with L-glutamine (25,030,081, Gibco), 10% FBS (10,500–064, Gibco) and pen-strep (15,140–122, Gibco). N2a cells were passaged 1:10 when the cells reached 80% confluency. Only N2a cells with a passage number between one to fifteen were used for this study. For expression of GFP and GFP-tagged constructs in N2a cells, 18 mm glass coverslips (Thermo Scientific) were placed in 12-well plates (Costar) and were coated with PDL (P7888, Sigma) at a concentration of 20 µg/ml for 30 min at RT. Excessive PDL was removed and 1 ml of growth medium was added to the wells. Subsequently, 100,000 cells were seeded onto the coverslip and incubated at 37°C. After 24 h of incubation, N2a cells reached a confluency of roughly 70%. Cells were then transfected using Lipofectamine 2000 (Invitrogen, cat # 11,668,019). 48 h post transfection N2a cells were fixed with pre-warmed (37°C) 4% PFA (104,005,100, Merck) for 30 min at RT. After washing 3 × with 1 × PBS cells were processed for immunostaining and further analysis.

Generation, characterization and maintenance of iPSCs

All subjects have provided written informed consent and generation of iPSC lines was approved by the Ethical Medical Committee of the University Medical Center Utrecht. Patients were diagnosed according to the diagnostic criteria for ALS (revised El Escorial). Controls were donors without a psychiatric or neurologic diagnosis (Supplementary material 15: Supplementary Table S6).

Primary human fibroblasts were acquired from skin biopsies of ALS patients carrying the C21orf2-V58L mutation and sex/age-matched, unrelated healthy controls. Information about the human iPSC lines used in this study can be found in Supplementary material 15: Supplementary Table S6 and these lines were generated at the MIND facility of the department of Translational Neuroscience, Brain Center, UMC Utrecht. Human dermal fibroblasts reprogramming was performed using the CytoTune®-iPS 2.0 Sendai Reprogramming Kit (Invitrogen, Waltham, MA, USA, Cat. No. A16517) that uses Sendai Virus Vectors encoding OCT3/4, SOX2, KLF4, and c-MYC, according to the manufacturer's protocol. Briefly, low passage ($P < 5$) human skin fibroblasts were plated at a density of 250,000 cells per well in a 6-well plate in DMEM GlutaMAX (Thermo-Fisher, 31,966–021), 10% FBS (Sigma, F7524), 1% pen-strep (Life Technologies, 15,140,122) and cultured at 37 °C with 5% CO₂. After 24 h, cells were transduced with a SendaiVirus vector expressing OCT4, SOX2, c-MYC and KLF4. After 7 days, human fibroblasts were dissociated and seeded on top of gamma-irradiated mouse embryonic fibroblasts and cultured in human embryonic stem cell (huES)

medium (DMEM-F12, 20% Knockout serum replacement (Life Technologies, 10,828,028), 0.5% pen-strep, 1% non-essential amino acids (NEAA; Life Technologies, 11,140,035), 1% L-Glutamine (Life Technologies, 25,030,024), 496 mM β-mercaptoethanol (Life Technologies, 21,985–023), 20 ng/ml human basic FGF (Pepro- tech, 100–188). After 2 to 4 weeks, iPSC colonies were manually picked for expansion and characterization.

The iPSC cell lines were cultured in feeder-free conditions on Geltrex™ LDEV-Free Reduced Growth Factor Basement Membrane Matrix-coated dishes (ThermoFisher Scientific, Waltham, MA, USA, Cat. No. A1413202) with StemFlex medium (Gibco™, Waltham, MA, USA, Cat. No. A33493-01 + A33492-01) and were maintained at 37 °C and 5% CO₂. Cells were kept in 2 cm petri dishes. iPSC lines were passaged once a week by incubating them with 0.5 mM EDTA in 1 × PBS (Gibco™, Waltham, MA, USA, Cat. No. 14190–094) for 1 min after being washed with 1 × PBS. Then, the EDTA was removed and cells were loosened from the plates by adding 100 µl StemFlex medium. Subsequently, 5 µl of this cell suspension was transferred to a new 2 cm petridish with StemFlex medium containing Rho-associated protein kinase (ROCK) inhibitor Y27632 (10 µM, Axon Medchem, Groningen, The Netherlands, Cat. No. 1683). The following day medium was changed to StemFlex and subsequently medium was changed every other day. iPSCs were characterized by performing immunocytochemical staining for pluripotency stem cell markers using the StemLight™ Pluripotency Antibody Kit (Cell Signaling, Danvers, MA, USA, Cat. No. 9656S), quantitative reverse transcription PCR (RT-qPCR) for gene expression analysis for pluripotency stem cell markers (relative to hUES6 line, Harvard University, RRID:CVCL_B194), karyotyping by G band staining to ensure normal karyotypes, and pluripotency assessment using the STEMdiff™ Trilineage Differentiation Kit (StemCell Technologies, Vancouver, Canada, Cat. No. 05230). Successfully reprogrammed clones were frozen and stored in liquid nitrogen. iPSCs were maintained in feeder-free conditions at 37 °C with 5% CO₂ and passaged once a week. Cells were tested for potential mycoplasma infection (Lonza Bioscience, LT07-318).

Differentiation of iPSC-derived human spinal motor neurons

iPSC differentiation into MNs was performed as described previously with minor modifications [97]. In brief, human iPSCs were plated in 6-well plates and kept in StemFlex medium for 48 h. Medium was switched to neural differentiation medium (NDM, DMEM-F12: Neurobasal (1:1) with 1% pen-strep, 1% NEAA, 1% L-Glutamine, 1% Sodium pyruvate, 1% N2 supplement, 2% B27 supplement) supplemented with ascorbic acid (AA),

SB431542, LDN, CHIR99021 (Sigma-Aldrich, SML1046) (NDM1). From day 7 to 12, NDM2 (NDM supplemented with AA, cAMP (Sigma-Aldrich, A6885), SB431542, LDN, CHIR, RA, Puromorphine) was added. At day 12, cells were washed once with PBS and incubated with Dispase (Bio-Connect, 07923) for 4 min at 37°C. Dispase was removed and cells were detached from the well with 1 ml of NDM3 (NDM supplemented with AA, RA, Puromorphine and cAMP) in order to obtain small cell clumps. Clumps were then transferred to non-coated 10 cm petri dishes (2–3 wells of a 6-well plate per 1×10 cm plate) in NDM3 medium. At day 18, aggregates in suspension were dissociated with Accutase (Innovative Cell Technologies, AT104) and 50,000–100,000 neurons were plated per well in a 12-well plate on glass coverslips (20 µg/ml PDL, 10 µg/ml Laminin-coated) in NDM4 (NDM supplemented with AA, BDNF, CNTF, GDNF, cAMP). Neurons were cultured for 3 days (neurite outgrowth analyzes) or up to 7 days for all other analyzes. For every assay at least 3 independent differentiations were generated per line. For proteasome inhibition MNs were treated with 100 nM of MG132 (dilution of 1:100 000 from stock Sigma-Aldrich M7449) for 3 h and directly fixed for further analyzes.

Co-immunoprecipitation in iPSC-derived motor neurons

For co-immunoprecipitation (IP), MNs were plated into 6 well plates at a density of 2×10^6 cells per well at the day 18 of the differentiation protocol and cultured for 7 days. At day 7, medium was removed and neurons were washed gently with 2 ml of ice-cold 1×PBS per well. All PBS was removed and neurons were from this point kept on ice. Neurons were lysed in 400 µl of lysis buffer (40 mM TrisHCl pH 7.5; 200 mM NaCl; 10% glycerol; 5 mM EDTA pH 8.0; 0.4% NP-40; 1×Protease inhibitor (Complete EDTA-free Roche Cat.no. 11873580001)). Lysates were incubated for 10 min at 4 °C on a rotating wheel and subsequently centrifuged for 10 min at 13,000 rpm. 60 µl of supernatant was transferred into a new Eppendorf tube and kept as an input sample for Western blot analysis. The rest of the supernatant was incubated for 1 h at 4 °C with 1 µg of mouse anti-C21ORF2 antibody (abcam ab167351) and 150 µg of magnetic Dynabeads Protein G (Thermo Fisher 10003D). Dynabeads were beforehand washed and blocked for 10 min in lysis buffer containing 0.2 mg/ml of Albumin from chicken egg white (CEA) (Sigma Cat.no. A5503-10G). After antibody incubation beads were held by a magnet and washed 3× with 500 µl of ice-cold lysis buffer. Afterwards all buffer was removed and beads with input samples were kept at -20 °C until use.

Western blotting

For Western blotting, MN lysates were prepared as described for co-immunoprecipitation. At day 7 after plating, 2×10^6 neurons in each well of 6 well plate were lysed in 400 µl lysis buffer. Neurons were lysed for 10 min and centrifuged for 10 min. Supernatant was transferred to new Eppendorf tube and 60 µl of a particular lysate was mixed with 20 µl of 4×NuPAGE LDS sample buffer (Invitrogen, NP0007) containing 10% β-mercaptoethanol. Samples were boiled for 5 min at 95 °C, 30 µl of boiled lysate was loaded per lane and separated in a SDS-PAGE polyacrylamid gel and transferred onto a 0.45 µm nitrocellulose membrane (Amersham Hybond-C Extra, GE Healthcare). After blocking in 0.01% Tween 20 in Tris-buffered saline (TBS-T) with 5% milk powder, membranes were incubated with primary antibodies ON at 4 °C. Primary antibodies used: anti-beta-Actin A2228 sigma Aldrich, anti-Ubiquitin MAB1510-I sigma Aldrich, anti-C21ORF2 27609-1-AP Proteintech, anti-NEK1 antibody (E-10): sc-398813 or anti-GFP A11122 Life Technologies. The next day, membranes were washed 3×5 min in TBS-T. Membranes were then incubated with peroxidase-conjugated secondary antibodies for 2 h at RT, washed 3×5 min in TBS-T and developed with SuperSignal West Dura Extended Duration Substrate (Pierce, Thermo Fisher Scientific). Images were acquired using a FluorChem-M imaging system (Protein Simple). Alternatively, Alexa 800 (Life Technologies, cat A32730, 1:10,000) was used as secondary antibody for double staining. Membranes were then imaged using an ODYSSEY Infrared imaging system. Signal quantification was performed using ImageJ/FIJI software. Mean intensity of individual bands was measured and normalized to β-ACTIN protein levels. Western blots from at least 3 independent experiments were analyzed.

Immunocytochemistry

Coverslips with human iPSC cells, human iPSC-derived MN, mouse primary cortical neurons or N2a cells were fixed in 4% PFA at RT for 30 min and then washed 3× with PBS and directly immunostained or stored at 4 °C until use. Samples were blocked using PBSGT solution for 30 min followed by incubation with primary antibodies diluted in PBSGT ON at 4 °C. Primary antibodies used: anti-C21ORF2 ab167351 abcam, anti-NEK1 A304-569A Bethyl Laboratories, anti-tubulin-beta-3 801201 BioLegend, anti-cleaved-Caspase-3 9661S CST, anti-phospho-Histone-HSA.X 02-636 Millipore, anti-CHAT AF3447 R&D Systems, anti-Ataxin2 611378 BD, anti-TDP-43 10782-2-AP ProteinTech, anti-UBQLN2 H00029978-m03 Abnova, anti-TBK1 sc-398366 Santa Cruz Biotechnology, anti-SOD1 ab13498 abcam, anti-OPTN ab23666 abcam, anti-Kinesin-5A ab5628 abcam

anti-FUS A300-293A Bethyl Laboratories, anti-C9ORF72 GTX632041 GeneTex, anti-TUBA4A T5168 Sigma Aldrich. The following day, coverslips were washed by 5× dipping in 100 ml of PBS-T and incubated with the secondary antibodies diluted in PBSGT for 1 h at RT or ON at 4 °C. Next, after 5 washes in PBS-T, cells on coverslips were incubated with DAPI for 10 min at RT. After 5 washes in PBS-T and one additional wash in PBS without detergent, coverslips were mounted on glass slides with FluorSave™ Reagent (Millipore, Cat. No. 345789).

RNA extraction, cDNA synthesis and quantitative RT-qPCR

Total RNA was isolated from pellets of 1.000.000 iPSC cells or iPSC-derived MNs using the RNeasy Mini Kit (50) (74,104, QIAGEN), according to the manufacturer's instructions. RNA quality and purity were analyzed in a NanoDrop. cDNA synthesis was conducted using the Superscript IV kit according to manufacturer's instructions. RT-qPCR was performed with a FastStart Universal SYBR Green Master (Rox) in a QuantStudio 6 Flex Real-Time PCR system (Applied Biosystems). Relative expression levels were determined using the ddCt method. *ACTINB* gene was used as reference for assessing the expression levels of target genes.

Proteomics

Cloning of GFP tagged constructs

Expression GFP tagged constructs for *FUS*, *KIF5A*, *TBK1*, *TUBA4A*, *C21orf2* and *NEK1* were created by cloning human cDNA into a pCX-GFP vector (kind gift of Prof. Alain Chedotal, Vision Institute, Paris, France) downstream of the *GFP* sequence. *FUS* cDNA was described previously [16]. *TBK1* cDNA was a kind gift of Nilo Riva and Dario Bonanomi (Istituto San Raffaele, Italy). *TUBA4A* cDNA was obtained from Sino Biological (cat #HG14067-G). *KIF5A* cDNA was a kind gift of Prof. Casper Hoogenraad (Utrecht University, the Netherlands). Furthermore, we used *C21orf2* NM_001271441.1 and *NEK1* NM_001199400 cDNAs.

Cell culture and transfection for proteomics

N2a cells were maintained in 75 ml flasks (Greiner CELLSTAR® T-75 flask) until they reached near confluence. Then cells were split into 4×15 cm dishes. These were then left to reach confluence for 48 h and then split in another 2 dishes each. In this way, 8×15 cm dishes were obtained with N2a cells ready to use for IP. 24 h later when cells reached app 50–70% confluency, cells were transfected. Four dishes with one of our GFP expression constructs and the other 4 with a pCX-GFP empty control vector using Lipofectamine 2000 (Invitrogen, cat # 11,668,019). The day after transfection, medium was refreshed. Transfection efficiency was estimated by

plating N2a cells on coverslips and transfecting cells with each GFP-tagged construct as was performed for co-IP. The percentage of GFP-positive cells was quantified after 48 h in 10 different optical fields per coverslip for each expression construct.

Immunoprecipitation for mass spectrometry

48 h after transfection, N2a cells were used for IP. Dishes were washed with 5 ml of ice-cold PBS and processed on ice at 4°C. Each dish was then lysed by scraping cells with a sterile cell-scraper into 3 ml of lysis buffer (described earlier). The cell lysates with same construct were pooled into a 15 ml Falcon. After an incubation of 10 min on a rotating wheel in the cold room, samples were centrifuged for 10 min at 13,000 rpm. Supernatants were then put in a new Falcon tube (60 µl were kept for Western blot analysis) and incubated for 1 h with 25 µl of GFP-Trap beads (Chromotek, cat gta-20) on a rotating wheel at 4°C. The Falcon tubes were centrifuged for 1 min at 400 rpm at 4°C to pellet the beads, supernatant was removed, and pelleted beads were resuspended in 100 µl of lysis buffer. 10 µl were kept for verification of co-immunoprecipitation by Western blots and the other 90 µl of bead suspension were transferred to a 1.5 ml Eppendorf. After 2 rounds of washing in 0.5 ml of ice-cold lysis buffer, all superfluous liquid was removed with a syringe with needle and the beads stored at -20°C until mass spectrometry analyses.

LC-MS/MS

Precipitated proteins were denatured and alkylated in 50 µl 8 M Urea, 1 M ammonium bicarbonate (ABC) containing 10 mM TCEP (tris (2-carboxyethyl) phosphine hydrochloride) and 40 mM 2-chloro-acetamide for 30 min. After fourfold dilution with 1 M ABC and digestion with trypsin (20 µg/200 µl), peptides were separated from the beads and desalted with homemade C-18 stage tips (3 M, St Paul, MN), eluted with 80% Acetonitrile (ACN) and, after evaporation of the solvent in the speedvac, redissolved in buffer A (0,1% formic acid). After separation on a 30 cm pico-tip column (75 µm ID, New Objective) in-house packed with C-18 material (1.9 µm aquapur gold, dr. Maisch) using a 140 min gradient (7% to 80% ACN, 0.1% FA), delivered by an easy-nLC 1000 (Thermo), peptides were electro-sprayed directly into a Orbitrap Fusion Tribrid Mass Spectrometer (Thermo Scientific). The latter was set in data dependent Top speed mode with a cycle time of 1 s, in which the full scan over the 400–1500 mass range was performed at a resolution of 240,000. Most intense ions (intensity threshold of 15,000 ions) were isolated by the quadrupole where after they were fragmented with a HCD collision energy of 30%. The maximum injection time of the ion trap was

set to 50 ms with injection of ions for all available parallelizable time. Raw data was analyzed with MaxQuant [version 1.6.1.0], using the *Mus Musculus* (taxonomy ID: 10,090) fasta file, extracted from UniprotKB. Oxidation of methionine and acetylation of the protein N-terminus were set as a variable, while carbamidomethylation of cysteine was set as a fixed modification.) The Tolerance for the first search was set to 20 ppm, which was lowered for the main search to 4.5 ppm. Peptide fragment tolerance was set on 0.5 Da.

The mass spectrometry proteomics data have been deposited with the ProteomeXchange Consortium via the PRIDE [98, 99] partner repository with the dataset identifier PXD051922.

Mass spectrometry analysis, selection of relevant interactors and interactome comparisons

We used the Perseus software platform (Tyanova et al., 2016) to analyse mass spectrometry results. For each bait protein, a scatterplot was created showing the median iBAQ intensity of proteins identified in the bait sample (GFP-tagged constructs) on the Y-axis versus the median iBAQ intensity of the proteins identified in the parallel control sample (GFP) on the X-axis. Proteins with the same intensity in the two samples that aligned along a diagonal continuous line in the centre of the scatterplot are considered background. To define the interaction intensity uniformly among different proteins, a cut-off of 4 times enrichment in the bait sample was used. Proteins selected above the cut-off were then categorized by their function using the PANTHER classification system (pantherdb.org). With the same program GO analysis was performed with a statistical test for overrepresentation of a biological process on each defined interactome. We then compared interactor lists with the tool InteractiVenn [100] and determined common interactors of our proteins. GO analysis for a biological process was performed also on the groups of shared proteins with PANTHER. Interaction network plots were created using the StringDB website (<https://string-db.org>) to identify interactions between proteins and Gephi website (<https://gephi.org>) to create a visualisation of the network.

Isogenic iPSC controls

Creation of isogenic lines using CRISPR/Cas9

To create an isogenic control line, we removed the nucleotide mutation from the genome of the iPSC line of Patient 1 using CRISPR/Cas9 technology. Our protocol is based on Santos et al., 2016 [56] with some changes. Protein SpCas9 was provided by Niels Geijsen, Leiden University Medical Center (<https://divvy.com/reagents/631>; [101]). Synthetic chemically modified guide sgRNA was produced by Synthego Corporation

(Redwood City, CA, USA). sgRNA sequence is 5'-GGG UAU CCC CCA ACG ACC GC-3' and it targets sequence of human *C21ORF2* gene in intron 4 at nucleotide position 44,332,787 (Homo sapiens GRCh38.81 chr21 *C21ORF2* ENSG00000160226). Wildtype donor DNA sequence flanking the target position (44,331,558 – 44,334,044) on each side was amplified from genomic DNA extracted from Control 1 iPSC line. The donor DNA sequence contained exon 4. Exon 4 contains the nucleotide mutation 44,333,234:C:A (Homo sapiens GRCh38.81 chr21 *C21ORF2* ENSG00000160226) leading to a C21ORF2-V58L protein mutation. The donor DNA sequence was cloned into vector pTox-hUNCX_Neo, a kind gift of Niels Geijsen. pTox-hUNCX_Neo is created from pDTA-TK vector from Addgene plasmid-22677 and contains a Neomycine resistance cassette. Donor DNA was subcloned into pTox-hUNCX_Neo removing DNA sequence for hUNCX, incorporating our donor DNA between the HindIII restriction site (1580) and the NdeI restriction site (6364). The Neomycine cassette from pTox-hUNCX_Neo (KpnI 3596 – BamHI 5357) was incorporated into our donor DNA at the target position of sgRNA mentioned before and created DNA donor vector pTox-hC21_Neo.

Electroporation of iPSC cells for creation of an isogenic control line

Cas9 protein was thawed at RT and sgRNA was thawed on ice. Plasmid was prepared with an endotoxin free maxiprep and was not linearized. iPSC cells at 80% confluency in a 2 cm dish (corresponding to approximately 2×10^6 iPSC cells) were detached from the dish by incubation with 0.5 ml of Accutase (Innovative Cell Technologies, AT104) for 10 min at 37 °C and collected into 5 ml of prewarmed 37 °C OptiMEM. Cells were not counted to minimize cell death, and cell number was estimated by quantification before the experiment. For each electroporation 100 µl of electroporation-mix was prepared (OptiMEM+1 µl sgRNA (stock 10 µg/ µl)+1 µl Cas9 (stock 12.5 µg/ µl)+5 µg DNA) in an Eppendorf tube. Cells were pelleted for 4 min at 200 rcf and supernatant was removed. The cell pellet was resuspended in 100 µl of electroporation mix. The cell suspension was transferred to electroporation cuvettes (EC-0002S, NEPA GENE). Electroporation was performed with a NEPA21 Type II electroporator. The settings used for electroporation were the same for all experiments; poring pulse 135 V (duration: 5 ms; interval: 50 ms; number of pulses: 2; decay: 10%; one direction) and transfer pulse 20 V (duration: 50 ms; interval: 50 ms; number of pulses: 5; decay: 40%; two directions). Immediately 1 ml of pre-warmed

StemFlex 37 °C was added into cuvette using pipet provided with cuvette. 200 µl, 300 µl and 500 µl of suspension with electroporated cells were plated per well in 12-well plate coated with Geltrex (LDEV-Free Reduced Growth Factor Basement Membrane Matrix, ThermoFisher Scientific, Waltham, MA, USA, Cat. No. A1413202) and containing 1 ml of pre-warmed StemFlex medium (Gibco™, Waltham, MA, USA, Cat. No. A33493-01 + A33492-01) with ROCK inhibitor Y27632 (10 µM, Axon Medchem, Groningen, The Netherlands, Cat. No. 1683). StemFlex medium was changed the next day. Cells were kept without selection agent for 4 days and at day 5 G418-Geneticin was added at a concentration 1000 µg/ml to remove all cells without donor DNA with Neomycine resistance. After selection, only few colonies appeared and these were analyzed for removal of the mutation. Genomic DNA was isolated from the cells and the DNA part containing exon 4 was amplified by PCR and sequenced. Clones in which the mutation was reversed were further characterized as described for other iPSC lines earlier.

Extraction of genomic DNA from iPSC cells

iPSC cells at 80% confluency in 2 cm petri dish corresponding to approximately 2×10^6 iPSC cells were washed with 2 ml of 1×PBS and incubated with 0.5 mM EDTA in 1×PBS (Gibco™, Waltham, MA, USA, Cat. No. 14190–094) for 5 min. Then, EDTA was removed and cells were detached from the plates by adding 1 ml of ice cold 1×PBS. Cells were collected in an Eppendorf tube and pelleted by centrifugation for 4 min at 200 rpm. Cell pellets were resuspended in 250 µl of SNET buffer (20 mM TrisHCl pH 8.0; 400 mM NaCl; 5 mM EDTA; 1% SDS) + 1.25 mg/ml ProteinaseK (Roche #20,425,900), vortexed and incubated for 20 min at 55 °C. Then the suspension was vortexed again, spun down and 125 µl of 5 M NaCl (-20 °C) was added. The suspension was placed on shaker for 10 min and then incubated on ice for 10 min. Afterwards the suspension was spun down for 10 min at 13,000 rpm at RT. 250 µl of supernatant were transferred to a new Eppendorf tube and 500 µl of ice cold 100% ethanol was added. After mixing the precipitated DNA was pelleted by centrifugation for 10 min at 13,000 rpm at 4 °C. Supernatant was removed and the pellet was washed with 250 µl 75% ethanol and centrifuged for 5 min at 13,000 rpm at 4 °C. All supernatant was removed, the pellet dried and resuspended in 30 µl of H₂O. DNA was used for PCR reactions for creating the donor DNA for the CRISPR/Cas9 protocol or for sequencing the exon4 of isogenic controls.

Analysis of neuronal morphology of MN

iPSC-derived MNs on glass coverslips were fixed and blocked after 3 days in culture. Then cells were incubated with the following set of primary antibodies: rabbit anti-beta-III tubulin (1:200, BioLegend, Cat. No. 801201, San Diego, CA, USA) and goat anti-Chat (1:200, Millipore, Burlington, MA, USA, Cat. No. AB144P) diluted in PBSGT ON at 4 °C. Coverslips were washed and incubated with donkey secondary antibodies: anti-rabbit AlexaFluor 488 (Life Technologies, Carlsbad, CA, USA, Cat. No. A21206) and anti-goat AlexaFluor 647 (Abcam, Cambridge, UK, Cat. No. AB150135) diluted 1:500 in PBSGT for 1 h at RT. Finally neurons were also stained with DAPI and mounted on glass slides with FluorSave™ Reagent (Millipore, Burlington, MA, USA, Cat. No. 345789).

For neurite outgrowth analysis, images were obtained using the Zeiss AxioImager M2 (Carl Zeiss AG., Oberkochen, Germany) with a 20X objective. For each experimental condition, an image that consisted of 100 tiles (10 by 10) was generated in the middle of the coverslip. To measure and quantify total neurite length, main axon length, and the number of branches per neuron, the MNs were traced and analysed using ImageJ/FIJI software and the NeuronJ plugin. Each TUBB3-channel image was optimized for tracing analysis by using the image adjust threshold tool. For every clearly identifiable individual MN, traces for every neurite were analyzed with the NeuronJ tracing tool. Four independent experiments were performed and for each cell line at least 40 neurons were analyzed. Statistical analysis was performed using GraphPadPrism.

Analysis of DNA damage in iPSC-derived MNs

MNs for DNA damage analyzes were cultured for 7 days as described earlier and treated with Neocarzinostatin for 1 h. MNs were then immediately fixed and immunostained with mouse anti-γH2AX (1:500; Millipore, cat #05–636) and goat anti-Chat (1:500; R&D Systems, cat AF3447) primary antibodies followed by donkey anti-mouse Alexa 568 (Life Technologies, cat A10037) and donkey anti-goat Alexa 647 (Abcam, cat ab150135) antibodies and stained with DAPI. (Merk, cat 345,789-20ML). Coverslips were mounted with FluorSave reagent and neurons were imaged using a confocal laser-scanning microscope (Olympus FV1000) with a 100X objective with 1024×1024 resolution and speed of 4 µs/pixel. Confocal microscope imaging settings (laser intensity, gain, pinhole) were maintained constant for all pictures taken. Neurons were scanned through the entire cell thickness and merged Z-stacks of the images were then analysed using the ImageJ/Fiji software. The DAPI channel was used to create ROIs used to measure γH2AX staining

intensity in the 568 channel. Three independent experiments were performed and at least 10 cells per condition per line were analyzed. All statistical analysis was performed in GraphPadPrism Software.

Analysis of mitochondria function in MN

Oxygen consumption rate (OCR) was analyzed in a XF24-3 Extracellular Flux Analyzer (Seahorse Biosciences). Human iPSC-derived MNs were plated in 24-well V7-PS plates (Seahorse Biosciences) at a density of 400,000 cells per well and used at DIV25 (cultured for 7 days after plating at day18 of differentiation). Four wells from each plate were left blank as background controls and at plate positions according to Analyzer protocol. For measurements, cells were gently washed 2× with 0.5 ml/well assay medium (50 ml Agilent Seahorse XF Base Medium (102,353–100), 20 mM glucose, 2 mM glutamine, 0.5 mM NaOH), put into fresh assay medium for at least 30 min, and assayed. For OCR analysis, three baseline recordings were made, followed by sequential injection of the ATP synthase inhibitor oligomycin, the mitochondrial uncoupler p-trifluoromethoxyphenylhydrazine (FCCP), and the mitochondrial complex 1 inhibitor rotenone and complex 3 inhibitor antimycin. For each assay, individual wells were examined after pre-measurement washes and after assays to ensure that cells did not detach and major cell death did not occur during the assay. Wells that did not fulfil these criteria were excluded from the analysis. Raw oxygen consumption rate values were used to calculate different bioenergetic parameters as described previously [102] and according to the manufacturer's guidelines. Data from 3 independent experiments and at least 3 replicates per line were quantified.

Patch-clamp electrophysiology

For recordings, 3 weeks-old cell cultures (DIV21 after plating at day 18 of the differentiation protocol) on coverslips were used and immersed in artificial cerebrospinal fluid (ACSF) containing (in mM): NaCl (124), KCl (2.5), glucose (11), HEPES (5), NaHCO₃ (26), NaH₂PO₄ (1), MgCl₂ (1.3), CaCl₂ (2.5). During recording cells were continuously superfused with ACSF at a flow rate of 2 ml/min at 32 °C.

Recordings were performed for cultures from all lines. For each of the lines, recordings were performed from 3 distinct batches (independent experiments, i.e. separate differentiations of MNs) of cultured cells. MNs were patch-clamped using borosilicate glass pipettes (2.7–4 MΩ; glass capillaries, GC150-10, Harvard apparatus, UK), under a BX51WI Olympus microscope (Olympus, France). Recordings were performed in current clamp using a potassium gluconate-based internal containing

(in mM), Potassium Gluconate 139; HEPES 10; EGTA 0.2; creatine phosphate 10; KCl 5; Na₂ATP 4; Na₃GTP 0.3; MgCl₂ 2. For current clamp recordings, signal was amplified, low-pass filtered at 2.9 kHz with a 4-pole Bessel filter and digitized at 20 kHz with an EPC9/2 dual patch-clamp amplifier (HEKA Elektronik GmbH, Germany). Data were acquired using PatchMaster v2×78.2 software. Cells were clamped at 0 pA for 400 ms in current clamp, then they were subjected to a specific current step of 800 ms, prior to a return to 0 pA holding currents for another 1000 ms. The current steps during the 800 ms window started at -20 pA, and upon each subsequent sweep increased with +5 pA compared to the previous step. A total of 24 sweeps were given, thus covering a current range from -20 to +95 pA. The inter-sweep interval was 10 s.

For biocytin labelling, 0.05% biocytin was added to the patch pipette medium. Subsequently the cover slip with cultured cells was fixed overnight in 4% PFA in a well plate. Subsequently PFA was removed by 3×15 min washes in PBS, followed by incubation in blocking solution (10% NGS, 0.5% Triton X-100) for 1 h at RT. Next, the coverslip was incubated with 555-conjugated streptavidin (1:500; Thermo Fischer Scientific, S21381, USA) in 2% NGS, 0.4% Triton X-100 in PBS overnight at 4 °C. Next, coverslips were washed in PBS for 3×15 min and mounted on glass slides and coverslipped using Fluor-Save (Millipore, 345,789, The Netherlands).

Electrophysiology data analysis and statistics

From the current–voltage relation data, excitability profiles and neuronal biophysical properties were calculated in Igor Pro-8 (Wavemetrics, USA). Excitability profiles were calculated as the number of action potentials (APs) generated during the 800 ms window of the 24 sweeps where currents were incrementally increased from -20 pA to +95 pA. Rheobase was calculated as the minimum current imposed to the cell to induce an AP. To determine AP threshold, we differentiated the rheobase sweep, calculated when voltage changes first occurred at a rate surpassing 20 mV/ms, and then related this timepoint in the original sweep to the matching membrane voltage. This voltage value was set as the AP threshold. Cells were considered spontaneously active if they fired at least 1 AP during the sweep where 0 pA was injected throughout. Membrane resistance was calculated with Ohm's law based on mild hyperpolarizing steps that did not lead to active conductance. In view of many spontaneously active neurons where active conductance occurred during 0 pA steps, resting membrane potential was not assessed.

Compiled data in bar graphs were always reported and represented as mean ± SEM, with single data points plotted (single cell). Continuous data were statistically

analyzed using One-Way ANOVA, unpaired t-test, two-way repeated-measures ANOVAs. For ANOVAs follow up post-hoc analyses were performed in case of a significant omnibus test, using Tukey's multiple comparison test. For non-parametric multi-group Boolean data, a Kruskal-Wallis test was used, followed up by Dunn's post-hoc comparison test. For non-parametric two group Boolean data we used a Mann-Whitney U test. Analyses were performed in GraphPad 9 (USA).

Zebrafish

Zebrafish maintenance & ethics statement

Fish were housed and handled according to local guidelines and policies in compliance with national and European law. All procedures involving experimental animals were approved by the local animal experiments committee, Koninklijke Nederlandse Akademie van Wetenschappen-Dierexperimentencommissie (AVD8010020173786). Adult zebrafish (*Danio rerio*) were maintained and embryos raised and staged as previously described [103]. Adult zebrafish were maintained in 4.5 L polyethylene tanks (Tecniplast) in an Aqua Schwarz holding system (Göttingen) supplied continuously with circulating UV treated filtered tap water, which was exchanged for 10–30% daily. Average water properties were: Nitrite 0.095 mg/L, Nitrate 16.7 mg/L, Chloride and Ammonium 0 mg/L, hardness 9.8 dH, pH 8.2, conductivity 460 mS, Oxygen 6.85 ppm and temperature 28.5 °C under cycles providing 14 h of light and 10 h of dark (14:10 LD; lights on 9 a.m.; lights off 11 p.m.).

Microinjection of zebrafish embryos

Overexpression constructs of human *C21ORF2-WT* or *C21ORF2-V58L* cDNA were cloned into a pCS2-GFP-2A plasmid, a kind gift of Prof Jeroen den Hertog (Hubrecht Institute, the Netherlands). mRNA for zebrafish injections was produced using mMACHINE SP6 Kit (AMBION, Life Technologies) following the manufacturer's instructions. pCS2 vector DNA was linearized using the NotI enzyme. 1 µg of linearized DNA was used for the reaction. RNA was purified by lithium-precipitation according to manufacturer's instructions. RNA was diluted in RNase free water to 0.05 µg/µl for the injections. Injection was performed using glass capillaries attached to WPI PV820 Pneumatic Pico Pump and Leica MZ 7.5 stereomicroscope. Settings of pump were adjusted to inject approximately 1 nl of mRNA solution. RNA was injected into one-cell stage zebrafish embryos.

Zebrafish developmental deformations and locomotor analysis

At 5 dpf zebrafish embryos were examined. Embryos with oedema, tail curvature or more severe deformations were

counted per total number of embryos in 5 independent experiments. For locomotor experiments only freely swimming embryos were used. Locomotor experiments were performed under dark conditions at 28 °C using 5 dpf embryos placed in a flat bottom 48-well cell culture plate filled with 1 ml E3 solution. Embryos were left to habituate for 20 min and then imaged for 1 h. Movements were tracked in an automated tracking device (ZebraBox™; Viewpoint, Lyon, France). Locomotor activity was quantified and analyzed by ZebraLab™ software by Viewpoint. Total distance and time spent swimming were recorded for each single embryo and results were analyzed in GraphPadPrism.

Whole-mount immunostaining of zebrafish embryos

Zebrafish were collected at 5 dpf and fixed in 4% PFA overnight at 4 °C. The day after fixation, embryos were washed 6×5 min in PBS-T (PBS+0.1% TritonX-100) and left to permeabilize for 90 min at RT in 1 mg/ml collagenase A (Roche, cat #10,103,578,001) diluted in PBS. Embryos were then washed 6×5 min in PBS-T and blocked in PBSGT+5% normal donkey serum (NDS) rotating ON at 4 °C. Embryos were then incubated with primary antibody mouse anti-SV2 (DSHB) 1:50 in 500 µl of PBSGT in an Eppendorf tube ON at 4 °C in a rotating wheel. Embryos were then gently washed 6×15 min in 2 ml PBS-T RT in a 2 ml Eppendorf tube on a bellydancer platform. Embryos were incubated with Donkey anti mouse-568 antibody and alfa-bungarotoxin-conjugated with Alexa488 (Thermo Fisher Scientific, cat B35451) both diluted 1:400 in 1 ml of PBSGT ON at 4 °C in a cold room on a rotating wheel and subsequently washed 6×15 min in 2 ml PBS-T RT gently in a 2 ml Eppendorf tube on a bellydancer platform. After being washed, embryos were mounted on glass slides with Fluorsave reagent (VWR, cat #345,789–20), using imaging spacers (PolyAn molecular surface engineering, cat #654,008) to protect fish from squeezing under the glass.

Analysis of zebrafish NMJ

To analyse the integrity of zebrafish embryo NMJs, 4 independent experiments were performed and at least 5 embryos per experiment and condition were imaged and analysed. The 17th-18th somites of 5 dpf zebrafish tails were imaged with a confocal laser-scanning microscope (Olympus FV1000). Merged Z-stacks of SV2 and BTX staining were analyzed in ImageJ/FIJI software and mean intensity for each channel in the entire image was measured. The resulting measurements were statistically analysed in GraphPadPrism.

For colocalization, Z-stacks were then analysed in Imaris software (Bitplane / <http://www.imaris.oxinst.com>). BTX staining, a marker for the postsynaptic

compartment, was transformed into “spots” with a dimension of 1 μm , background correction and the use of automatic “quality” threshold. A mean staining intensity threshold and a Y-position threshold were also used to eliminate the bottom of the fish, where specks of antibodies tended to collect. SV2, a marker for the presynaptic compartment, was transformed in “surfaces” using background correction and an automatic threshold. The same Y-position threshold was also used to define the surfaces. We then used the function “spots close to surfaces” with a distance threshold set at 0.05 μm to define the amount of BTX spots colocalizing with the SV2 surfaces. We used GraphPadPrism (<https://www.graphpad.com/scientific-software/prism/>) to do statistical analysis.

Microscopy and image analysis

Fluorescence microscopy was performed with an upright ZEISS Axio Imager 2 Upright Microscope equipped with an AxioCam Icc 3 camera, and LD Plan-Neofluar 20x/0.4Korr objective using the ZEN software (Zeiss). Confocal microscopy was performed with a laser-scanning microscope Olympus FluoView FV1000 equipped with objectives UPLSAPO 10X 2, UPLSAPO 20x, UPLSAPO 40x2, UPLSAPO 100xO and AxioVision software. Image analysis was performed using ImageJ/FIJI or for Zebrafish SV2/BTX colocalisation in Imaris software (Bitplane / <http://www.imaris.oxinst.com>).

To analyse soma size, nucleus size and the signal intensity for expression of a particular protein in individual neurons in immunostaining, the merged z-stacks of confocal images in the channel of interest were opened in ImageJ/FIJI software. The area and the immunostaining signal (mean intensity) were measured for the neuronal soma or nucleus by creating a ROI using thresholded CHAT (soma) or DAPI (nucleus) channel. 3 independent experiments were performed and at least 10 neurons per line were analyzed.

To analyze neuronal apoptosis, the number of cCAS3-positive neurons were counted in 20x images obtained with the ZEISS Axio Imager 2 and divided by the total number of neurons (CHAT-positive) per each optical field. 3 independent experiments were performed and at least 10 neighbouring optical fields covering more than 100 neurons per line were analyzed.

General statistical analysis

Statistical analysis was performed in GraphPadPrism version 9.5.1. (<https://www.graphpad.com/scientific-software/prism/>). Datasets were tested for normality and differences in variance between groups to determine the appropriate statistical test. If not stated differently the following statistical tests in GraphPadPrism were used:

to compare two independent groups, unpaired t-test in case of normally distributed data and nonparametric Mann–Whitney test in case of non-normal distribution, one-way ANOVA followed by the Tukey’s correction for multiple comparisons was used to evaluate differences among multiple groups if data were normally distributed, otherwise the Kruskal–Wallis test followed by Dunn’s multiple comparison test was used. Each test applied in experiments are stated in the figure legends. All statistical significance was ranked as the following: * $P < 0.05$; ** $P < 0.01$; *** $P < 0.001$ and **** $P < 0.0001$.

Results

Interactome analysis of recently identified ALS-associated proteins

To further dissect the disease mechanism underlying ALS and to identify potential unique or common disease pathways that are suitable for therapeutic intervention, we performed comparative interactome analyses of 5 recently identified ALS-associated proteins (C21ORF2, KIF5A, NEK1, TBK1, TUBA4A). FUS was included to allow comparison to previous studies in which we performed similar interactome studies of FUS and other proteins [15, 16]. GFP-tagged proteins were expressed in N2a cells followed by pull down and mass spectrometry (Fig. 1A–H). Importantly, GFP-tagged proteins exhibited a subcellular distribution similar to those reported for their endogenous counterparts. Quantification of the transfection efficiency of the different GFP-tagged proteins showed GFP expression in 49–73% of cells (C21ORF2 73%, FUS 70%, KIF5A 55%, NEK1 49%, TBK1 54%, TUBA4A 71%) (Fig. 1B–H). Bait proteins were captured using GFP beads and pulldown efficiency and specificity were confirmed using Western blot before mass spectrometry (Supplementary material 1: Supplementary Fig. S1A–F). Each GFP-tagged bait protein was processed in parallel to a GFP control, and proteins that were at least 4 times more abundant in bait as compared to control samples were considered as interactors (Fig. 2A–F). With these criteria, 176 interactors for C21ORF2, 182 for FUS, 36 for KIF5A, 35 interactors for NEK1, 74 interactors for TBK1, and 188 interactors for TUBA4A were identified. It should be noted, however, that the relatively low expression of the bait proteins and our rather stringent criteria for the selection of interactors may have precluded the selection of weaker interactors. The selected interactors included both known and novel binding partners or indirect interactors of the different baits. Interactors were classified according to their reported functions using GO analysis (PANTHER software; pantherdb.org) (Fig. 2A–F). In line with our previous observations,

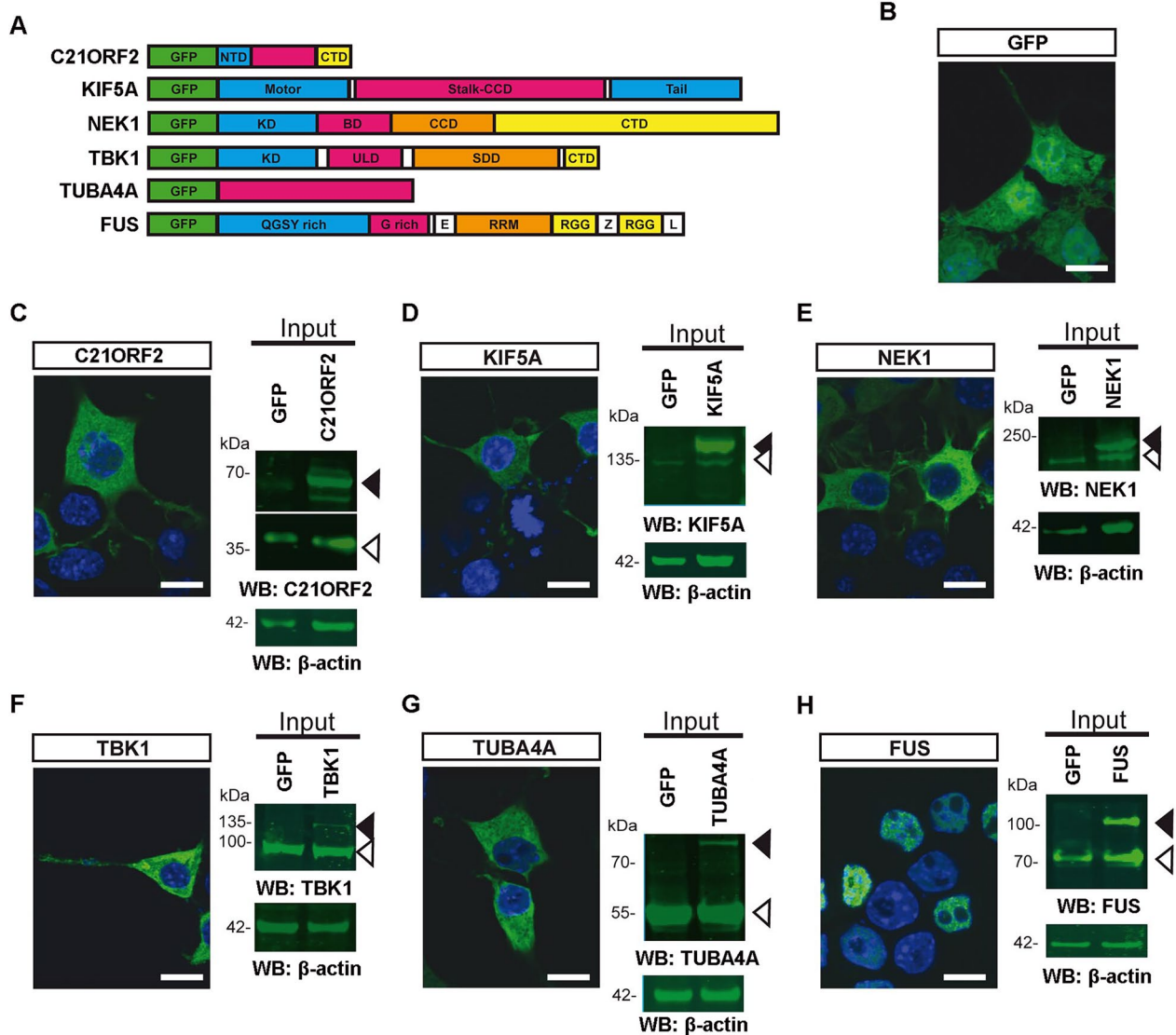


Fig. 1 Expression analysis of bait proteins for interactome analysis. **A** Schematic representation of GFP-tagged C21ORF2, KIF5A, NEK1, TBK1, TUBA4A and FUS. *NTD*—N-terminal domain; *CTD*—C-terminal domain; *CCD*—coil-coiled domain; *KD*—kinase domain; *BD*—basic domain; *ULD*—ubiquitin-like domain; *SDD*—scaffold and dimerization domain; *QGSY*—Glu-Gly-Ser-Tyr-rich region; *G rich*—Gly-rich region; *E*—nuclear export signal; *RRM*—RNA recognition motif; *RGG*—Arg-Gly-rich region; *Z*—zinc finger motif; *L*—nuclear localization signal. **B–H** Left panel: Expression of GFP and GFP-tagged proteins in Neuro2A (N2a) cells assessed by immunohistochemistry (DAPI in blue). Exogenous proteins show an endogenous distribution pattern. **C–H** Right panel: Western blots showing GFP-tagged (black arrowhead) and endogenous (white arrowhead) proteins. Anti-β-actin is used as loading control. Scale bar B–H: 5 μm

interactors of FUS included DNA/RNA binding proteins, DNA/RNA helicases, Elavl proteins, hnRNPs, snRNPs and ribosomal proteins (Fig. 2F; Supplementary material 10: Supplementary Table S1A–C) [15, 16]. This confirmed our ability to replicate previous results and the reliability of the interactome data. Below, each of the interactomes identified in this study is discussed in more detail.

C21ORF2

C21ORF2 (or cilia- and flagella-associated protein 410 (CFAP410)) was previously associated with primary cilia formation and DDR [26–29]. Our results significantly expand our understanding of C21ORF2 interaction partners and potential functions (Fig. 2A). A large group of interactors were proteins with chaperone/

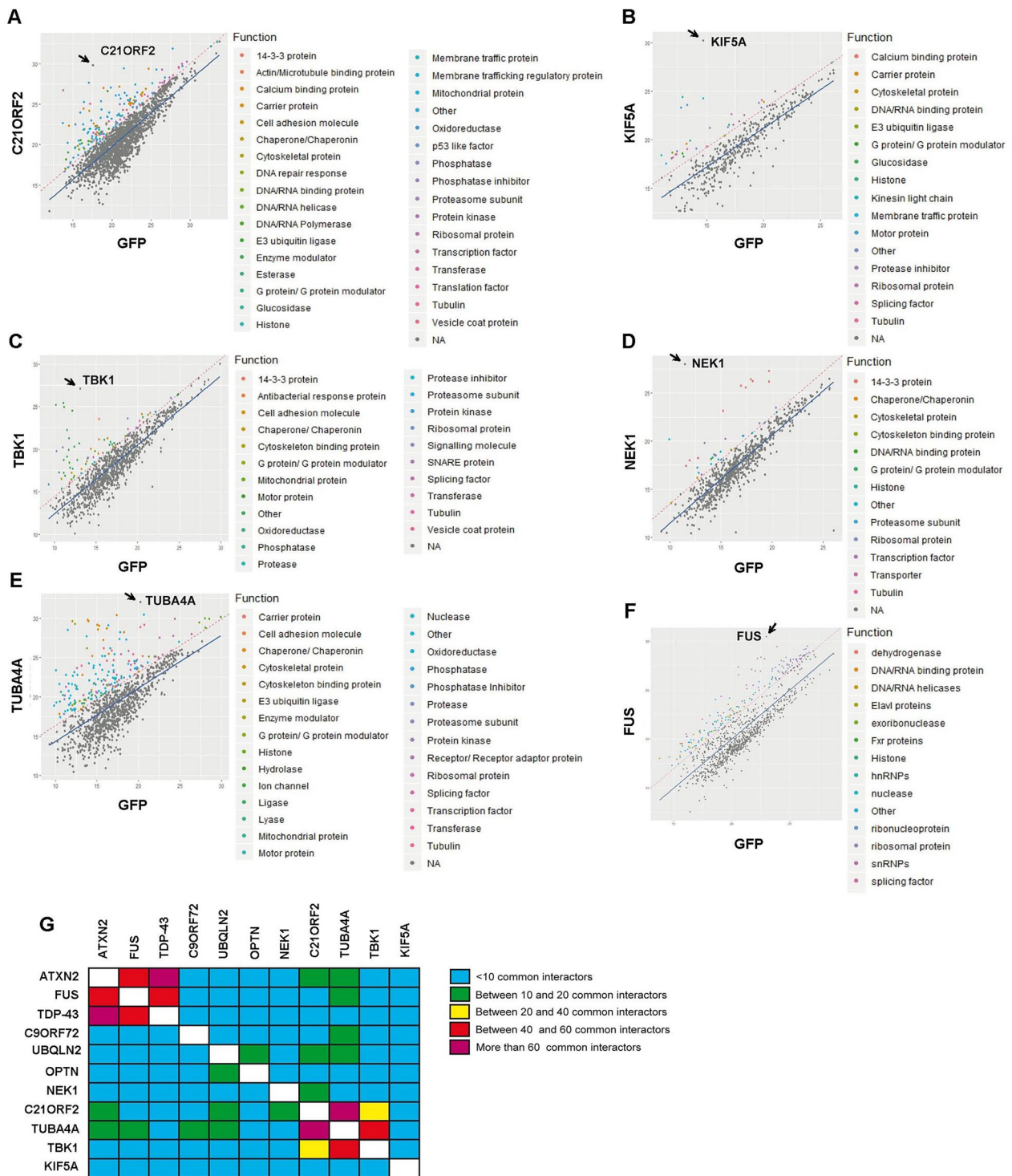


Fig. 2 Analysis of the binding partners of six ALS-associated proteins. **A–F** Scatter plots showing the interactors of the indicated bait proteins. Each graph shows all proteins identified in the GFP-tagged protein sample (y-axis) versus proteins in a corresponding GFP control sample (x-axis). Each protein is plotted according to its intensity value (abundance) in the sample. The blue line represents the intensity value that is the same for both GFP-tagged protein and GFP control samples. The red line indicates the cutoff used (4 times enrichment in the GFP-tagged sample) to detect probable interactors. These interactors are also colored according to their predicted function (GO analysis using PANTHER software). For each graph the position of the GFP-tagged (bait) protein is indicated (arrow). **G** Heatmap summarizing the shared interactors of 11 ALS-associated bait proteins analyzed in the current study and our previous work (Blokhuys et al., 2016)

chaperonin function. Other prominent groups were comprised of ribosomal proteins, cytoskeletal proteins, 14–3-3 proteins, DNA/RNA metabolism proteins, phosphatases and kinases (Supplementary material 11: Supplementary Table S2A). GO Biological Process analysis showed overrepresentation of proteins with chaperon function involved in various processes such as aggrephagy, protein folding, chaperon mediated autophagy and localization of proteins/RNA to telomeres (Supplementary material 12: Supplementary Table S3A).

KIF5A

KIF5A is a kinesin heavy chain subunit of the kinesin motor complex involved in anterograde transport that is essential for axon maintenance [38, 39]. While mutations in the KIF5A N-terminal motor domain are associated with the neurodegenerative diseases hereditary spastic paraplegia (SPG10) and Charcot Marie-Tooth type 2 (CMT2), mutations in the C-terminal cargo-binding domain are linked to ALS [18, 19]. Our interactome study identified proteins of the kinesin protein complex and cytoskeleton in addition to histone subunits and ribosomal proteins (Fig. 2B; Supplementary material 11: Supplementary Table S2B). GO Biological Process analysis highlighted the role of KIF5A in axonal transport (Supplementary material 12: Supplementary Table S3B).

TBK1

TBK1 is a protein kinase with well-described roles in inflammatory response, innate immunity and autophagy [40, 41, 42]. Our pull-down study identified several known TBK1 interactors, including TANK, AZI2 and TBKBP1. These are TBK1 adapter proteins and mediate TBK1 binding to different protein complexes [43]. Novel interaction partners included proteins with chaperone/chaperonin function, 14–3-3 proteins, mitochondrial proteins, ribosomal proteins and tubulin proteins (Fig. 2C; Supplementary material 11: Supplementary Table S2C). GO Biological Process analysis identified mitochondria metabolism and mitophagy, chaperon/chaperonin function regulating the localization of proteins to telomeres and aiding protein-complex formation (Supplementary material 12: Supplementary Table S3C).

NEK1

NEK1 is a member of the NIMA-related kinase family of proteins with various roles in the cell cycle [44, 45]. NEK1 was previously associated with primary cilia formation [46–49] and DDR [33, 34, 50] and is known to interact with C21ORF2 [26, 27, 51, 52]). As predicted, the NEK1 interactome contained C21ORF2 in addition to 14–3-3

proteins and a few ribosomal proteins, transcription factors, importins and histone proteins (Fig. 2D; Supplementary material 11: Supplementary Table S2D). The overall enrichment of proteins into pathways was low, but GO analysis identified protein folding, protein targeting, ribonucleoprotein complex assembly and organization, translation and peptide metabolism (Supplementary material 12: Supplementary Table S3D).

TUBA4A

TUBA4A is part of the alpha tubulin family, which together with beta tubulins compose the structure of microtubules [53]. The large TUBA4A interactome consisted of proteins with diverse functions. As expected, TUBA4A pulled down other members of the tubulin family and transport-related motor proteins (Fig. 2E; Supplementary material 11: Supplementary Table S2E). Potential novel interactors included mitochondrial proteins, proteins with chaperone/chaperonin function, proteasome proteins, ribosomal proteins, histone proteins, transcription factors and diverse groups of proteins with various functions (Supplementary material 11: Supplementary Table S2E). GO Biological Process analysis revealed an enrichment of proteins connected to mitochondria-related functions, like oxidative phosphorylation and nitrosative stress-induced apoptosis. The other enriched group of proteins was connected to chaperone functions such as localization of proteins/RNA to the telomere, regulation of aggrephagy, protein folding and chaperone-mediated autophagy (Supplementary material 12: Supplementary Table S3E).

Comparison of different interactomes reveals distinct and shared pathways

Our previous work showed that comparison of the interactomes of different ALS-associated proteins can identify common (disease) pathways and targets, such as FMRP [16]. To further explore the existence of shared pathways downstream of different ALS-associated proteins, we compared the interactomes identified here with those reported in our previous study (C21ORF2, KIF5A, TBK1, NEK1, TUBA4A, FUS, ATXN2, TDP-43, C9ORF72, UBQLN2, OPTN). Although different pull-down methods were used in both studies, comparison of the reported FUS interactomes revealed a significant overlap in interactors and pathways (Fig. 2F; Supplementary material 10: Supplementary Table S1A–C) [16]. This observation indicated that we could compare data of our current and previous work. Re-analysis of all data confirmed our previous observations that the interactomes of FUS, ATXN2 and TDP-43, and of UBQLN2 and OPTN display significant overlap (Fig. 2G) [16]. We also identified shared interactors for other combinations of

ALS-associated proteins, including overlap between the interactomes of C21ORF2, TBK1 and TUBA4A (Fig. 2G; Supplementary material 13: Supplementary Table S4A; Supplementary material 2: Supplementary Fig. S2A, C), with 20 proteins found to bind all three baits. Most of these proteins had chaperone/chaperonin functions (CCT2, CCT6a, CCT8, CDC37, HSP90AA1, HSP90AB1, HSPA5, HSPA8, STIP1) or belonged to the tubulins (TUBA1B, TUBB2B, TUBB3, TUBB4B) (Supplementary material 13: Supplementary Table S4A; Supplementary material 2: Supplementary Fig. S2A, C). Interestingly, C21ORF2 also shared a significant number of interactors with NEK1 (Fig. 2G; Supplementary material 13: Supplementary Table S4B; Supplementary material 2: Supplementary Fig. S2B, D). C21ORF2 and NEK1 bound each other in addition to 11 other shared interactors. This included 6 out of 7 existing 14–3–3 proteins: YWHAB, YWHAE, YWHAG, YWHAH, YWHAQ, YWHAZ (Supplementary material 13: Supplementary Table S4B; Supplementary material 2: Supplementary Fig. S2B, D). No significant overlap of KIF5A interactors with interactors

of other baits was identified. Overall, our data identify two larger hubs of shared interactors: one consisting of FUS-ATXN2-TDP-43, sharing proteins involved in RNA metabolism; and another formed by C21ORF2-TBK1-TUBA4A, sharing mostly proteins with chaperone function involved in protein quality control.

C21ORF2 is strongly expressed in ALS relevant neurons

Molecular pathways shared by different ALS-associated proteins provide an opportunity to further understand the disease mechanisms underlying ALS. To exploit this opportunity, we focused on C21ORF2 as it bound NEK1 [51, 52, this study] and shared a relatively high number of interactors with several other ALS-associated proteins (NEK1, TBK1, TUBA4A). The function(s) and neuronal expression pattern of C21ORF2 remain poorly understood. Therefore, immunohistochemistry was used to examine whether C21ORF2 is expressed in ALS relevant neurons. C21ORF2 showed strong expression in deep layer CTIP2-positive neurons in mouse motor cortex and in CHAT-positive mouse spinal MNs (Fig. 3A).

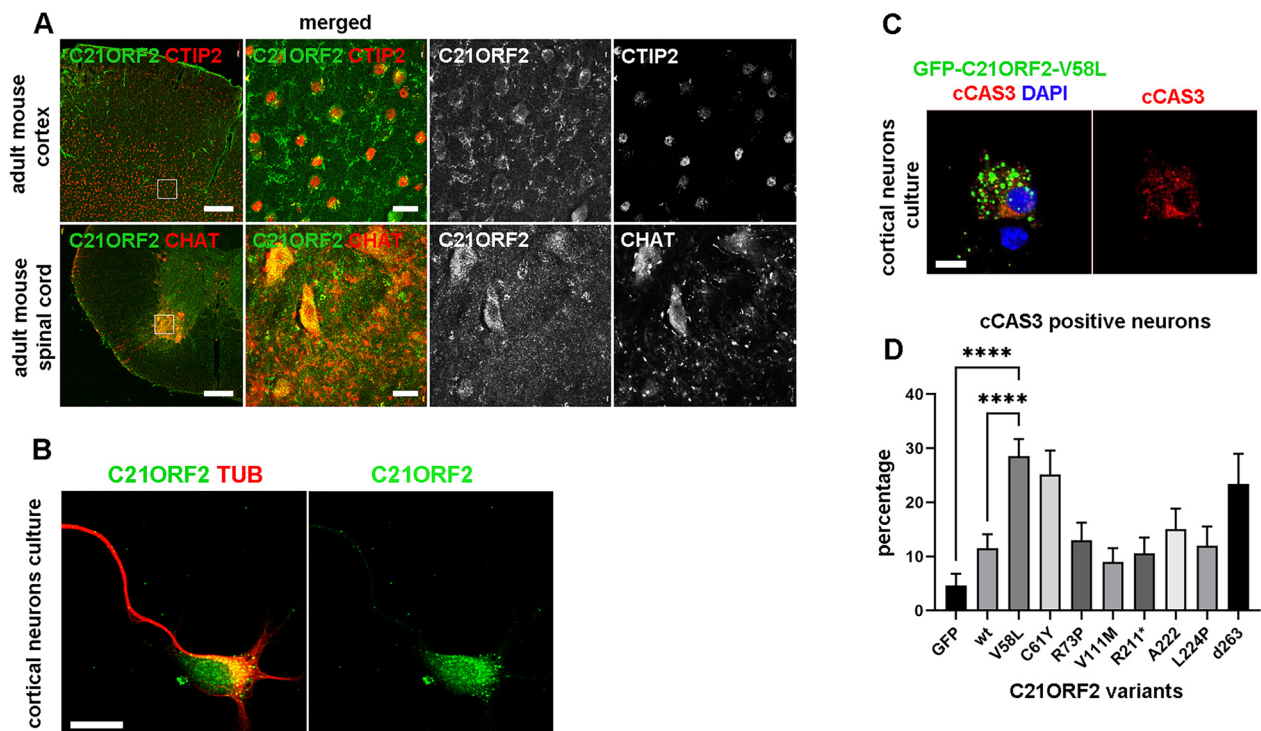


Fig. 3 ALS-associated C21ORF2 variants cause neuronal apoptosis. **A** Coronal sections of adult mouse motor cortex and spinal cord were co-immunostained for C21ORF2 and CTIP2 (upper panel) or CHAT (lower panel) to mark upper and lower MNs, respectively. Squares in left panels are shown at higher magnification in the right three panels. **B** Co-immunostaining for C21ORF2 and tubulin of mouse primary cortical neurons at 5 days in vitro (DIV). **C** Immunostaining for C21ORF2 and cleaved-Caspase-3 (cCAS3) of DIV5 mouse primary cortical neurons exogenously expressing C21ORF2-V58L. **D** Quantification of the percentage of cCas3-positive primary cortical neurons in cultures expressing GFP, GFP-tagged wild type C21ORF2 or GFP-tagged C21ORF2 variants. C21ORF2 variants are related to ALS (V58L, R211*, A222, d263), ciliopathies (L224P, C61Y) or both (R73P, V111M). Results from three independent experiments are plotted as means with SEM. **** $P < 0.0001$ Kruskal–Wallis test, Dunn’s multiple comparison post-hoc test. Scale bars: A, 200 μ m (low magnification); 20 μ m (high magnification); B, 10 μ m; C, 5 μ m

Analysis of the subcellular distribution of C21ORF2 by immunostaining of mouse primary cortical neurons or by using GFP-tagged C21ORF2 in N2a cells revealed a predominant cytoplasmic distribution with weak expression in the nucleus (Fig. 3B; Supplementary material 3: Supplementary Fig. S3A). To further study this distribution pattern, protein structure prediction software <http://raptorx6.uchicago.edu/> [54] was used and shows that C21ORF2 contains three major domains, in addition to nuclear localization and export signals (NLS and NES, respectively) (Supplementary material 3: Supplementary Fig. S3B-C) similarly to previously described C21ORF2 structure [52, 55]. C21ORF2 contained a highly structured N-terminal domain (aa 1–142; NM_001271441.1; NP_001258370), a low complexity middle domain (aa 143–213), and a C-terminal domain (aa 214–376). The expression data suggested that C21ORF2 may shuttle between the cytoplasmic and nuclear compartments and indeed deletion of its C-terminal domain, and thus the NES, led to accumulation of C21ORF2 protein in the nucleus (Supplementary material 3: Supplementary Fig. S3A). Overall, these data show that C21ORF2 is expressed in both cytoplasmic and nuclear compartments and in upper and lower MNs, which are affected in ALS.

C21ORF2-V58L causes apoptosis, reduced mitochondrial activity and impaired DNA damage response

Mutations in *C21ORF2* have been linked to ciliopathies and/or ALS. To study how these mutations affect neurons, GFP-tagged *C21ORF2* expression constructs were generated carrying one of 8 different mutations that are associated with ALS (<http://databrowser.projectmine.com/>), ciliopathies or both (Supplementary material 14: Supplementary Table S5). This selection was based on literature [27–29] or on the predicted detrimental effect and abundance of mutations in ALS [17, <http://databrowser.projectmine.com/>]. Although all mutant

C21ORF2 proteins showed wildtype distribution patterns (Supplementary material 3: Supplementary Fig. S3D), expression of C21ORF2-V58L induced a significant increase in the number of apoptotic neurons, as marked by cleaved-caspase-3 immunostaining (Fig. 3C, D).

To further understand the potential pathogenic effects of this variant in the context of ALS, C21ORF2-V58L was selected for further analysis and fibroblast-derived iPSC lines were generated from ALS patients carrying C21ORF2-V58L mutations and from age/gender matched controls. One patient (P1) carried a heterozygous *C21ORF2-V58L* mutation and the other patient (P2) two different *C21ORF2* mutations on separate alleles (*C21ORF2-V58L* and *C21ORF2-R60W*) (Supplementary material 4: Supplementary Fig. S4A-D; Supplementary material 15: Supplementary Table S6). MN cultures were generated using established protocols (Du et al., 2015; Supplementary material 4: Supplementary Fig. 4E) and analyzed using various molecular and cellular approaches. First, we showed that C21ORF2 mRNA or protein expression was unchanged in C21ORF2-V58L MN cultures (Fig. 4A-E). Similarly, cell and nucleus size, and neurite outgrowth and branching were comparable in mutant and control cultures (Supplementary material 5: Supplementary Fig. S5A-G). In contrast, ALS mutant cultures displayed a significant increase in the number of CHAT-positive MNs showing cleaved-Caspase-3 staining at days in vitro (DIV)25 (Fig. 4F-G), in line with the analysis of primary mouse cortical neurons that expressed *C21ORF2-V58L* constructs (Fig. 3C, D). Analysis of mitochondrial activity using the Seahorse XF analysis system showed a decrease in maximum respiration and spare respiratory capacity in C21ORF2-V58L MNs as compared to control cultures (Fig. 4H-J). Finally, the DDR was analyzed, given the reported role of C21ORF2 in DNA damage repair. To induce DNA damage, MN cultures were treated with Neocarzinostatin (0.1 µg/ml) for 1 h and stained for γH2AX protein, a

(See figure on next page.)

Fig. 4 C21ORF2-V58L causes apoptosis, reduced mitochondrial activity and impaired DNA damage responses. **A–L** Expression and functional analysis of iPSC-derived motor neuron (MN) cultures at days in vitro 25 (DIV25, 7 days after plating). C1 and C2, healthy controls; P1, ALS patient with C21ORF2-V58L mutation; P2, ALS patient with C21ORF2-V58L/C61Y mutations. **A–E** C21ORF2 protein and mRNA expression is unchanged in mutant MNs **A, B** Co-immunostaining for CHAT and C21ORF2 in control and mutant. **B** Quantification of immunostainings as in **A**. **C** RT-qPCR analysis of *C21ORF2* gene expression in control and mutant MNs. For relative mRNA expression the ΔCt values ($\Delta\text{Ct} = \text{Ct}(\text{C21ORF2}) - \text{Ct}(\text{ACTINB})$) for each line are shown. **D, E** Western blot analysis using anti-C21ORF2 and anti- β -ACTIN antibodies. β -ACTIN was used as loading control. **D** Representative Western blot. **E** Quantification of C21ORF2/actin intensity ratio in Western blot experiments as in **D**. **F, G** The number of cCas3-positive MNs is increased in mutant cultures. **F** Co-immunostaining for cleaved-caspase-3 (cCas3) and CHAT in control and mutant cultures. **G** Quantification experiments as in **F**. **H** Representative kinetics graphs of mitochondrial oxygen consumption in cultures. **I, J** Quantification of maximum respiration and spare respiratory capacity, both of which show a significant reduction in mutant cultures. **K, L** Co-immunostaining for CHAT and γ H2AX, a marker of the DNA damage response, after 1 h of neocarzinostatin (NCS) treatment. **L** Quantification of γ H2AX staining intensity in MN nuclei after NCS treatment, showing a significant decrease in mutant MNs. **B–E, G, I, J, L** Results of at least three independent experiments are plotted as means with SEM. * $p < 0.05$; ** $p < 0.01$; **** $p < 0.0001$, **G, I, J, L** Kruskal-Wallis test, Dunn's multiple comparison post-hoc test. Scale bars: **A**, 10 µm; **F**, 100 µm; **K**, 5 µm

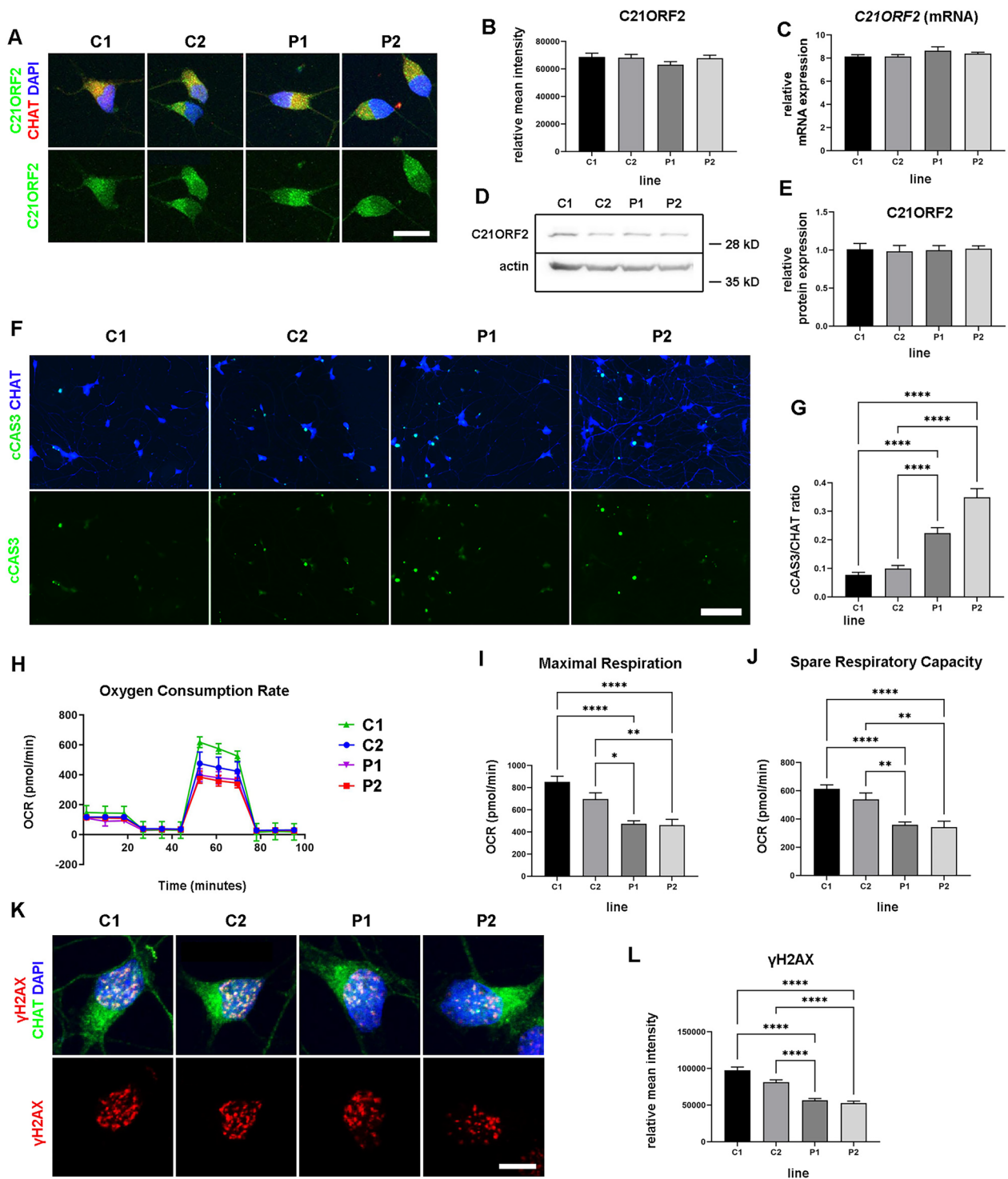


Fig. 4 (See legend on previous page.)

marker of DNA damage. Neocarzinostatin causes DNA damage and γ H2AX is recruited to the site of DNA breaks. Staining for γ H2AX was decreased in nuclei of C21ORF2-V58L MNs (Fig. 4K, L), suggesting a slower

or weaker response to DNA damage. In all, these results show that iPSC-derived MNs carrying the C21ORF2-V58L mutation show increased apoptosis, reduced mitochondrial activity and impaired DDR.

To firmly establish that these defects were caused by the *C21ORF2-V58L* mutation, an isogenic control line was generated from the P1 line using a combination of Cas9 purified protein, short guide RNAs and donor DNA (Supplementary material 6: Supplementary Fig. S6A-C) [56]. Two isogenic clones were generated which showed similar characteristics with respect to karyotype, expression of pluripotency markers in iPSCs and *C21ORF2* expression in iPSC-derived MNs. Therefore, one of the clones (Iso1) was used for further experiments. Iso1-derived MNs did not show changes in *C21ORF2* mRNA or protein expression, as compared to MNs generated using its parental line (P1) or control (C1) (Supplementary material 6: Supplementary Fig. S6D-H). Next, the phenotypes described above were studied in MN cultures derived from the isogenic control line. The increase in apoptosis and decrease in maximum respiration and spare respiratory capacity were rescued in isogenic control cultures (Fig. 5A-E). Finally, γ H2AX staining showed that the DDR was rescued in isogenic control as compared to P1 MNs (Fig. 5F-G). Together, these data show that the *C21ORF2-V58L* mutation causes several cellular phenotypes in patient-derived MN cultures.

C21ORF2-V58L affects motor neuron function

To examine whether the *C21ORF2-V58L* mutation also influence MN function, we evaluated the electrophysiological excitability profile of iPSC-derived MNs from healthy controls and ALS patients. MNs were patch clamped in whole-cell current clamp mode (Fig. 6; Supplementary material 7: Supplementary Fig. S7A) and subjected to increasing amounts of depolarizing current while their action potential (AP) output was monitored. As current intensity increased, *C21ORF2-V58L* MNs produced fewer APs as compared to control MNs (Fig. 6A, B; Supplementary material 7: Supplementary Fig. S7B, C). Isogenic control (Iso1) MNs exhibited more AP output in response to lower current injections as compared to MNs generated from the parental mutant line. This effect was, however, less pronounced at higher current intensities (Fig. 6B, C).

Many of the recorded MNs exhibited spontaneous activity in the absence of stimulation. Analysis of differences in the rheobase, the minimal current required to elicit the first AP, revealed a lower rheobase in mutant MNs. However, this difference was only statistically significant for the C2 to P2 comparison and no rescue was observed in Iso1 MNs (Fig. 6D; Supplementary material 7: Supplementary Fig. S7D). Analysis of the actual percentage of spontaneously active cells in the complete absence of stimulation showed that mutant cultures (P1 and P2) had a significantly higher incidence of spontaneously active MNs as compared to control (C1 and C2) (Fig. 6E; Supplementary material 7: Supplementary Fig. S7E). In isogenic control (Iso1) cultures, this phenotype was not fully rescued as it was not significantly different from P1 data (Fig. 6E). Finally, different biophysical membrane parameters were assessed. Membrane resistance was not significantly different and other parameters differed between lines. Mutant MNs showed lower membrane capacitance and a smaller AP after hyperpolarization. However, these effects were not significantly rescued by the isogenic control (Supplementary material 16: Supplementary Table S7).

Overall, these results show that although *C21ORF2-V58L* MNs are more spontaneously active (in the absence of stimulation), they show a lower capacity of further increases in their firing frequency upon stimulation.

C21ORF2-V58L affects motor behavior of zebrafish embryos

To explore whether the *C21ORF2-V58L* mutation also impacts the motor system in vivo, zebrafish embryos were used. GFP (control) and GFP-tagged human wildtype (WT) or mutant *C21ORF2* (V58L) protein were expressed by mRNA microinjection at the one-cell stage [16]. Non-injected embryos were used as an additional control. Expression of *C21ORF2-WT* or *C21ORF2-V58L* led to an increased number of deformed embryos (approx. 20% and 30%, respectively; Fig. 7A, B). The deformation included pericardial oedema and curvature of the tail, defects that have previously been linked to cilia dysfunction in zebrafish [57–59]. These results suggest

(See figure on next page.)

Fig. 5 *C21ORF2-V58L* mutant phenotypes are rescued in isogenic control cultures. **A–G** Functional analysis of iPSC-derived motor neuron (MN) cultures at days in vitro 25 (DIV25, 7 days after plating). C1, healthy control; P1, ALS patient with *C21ORF2-V58L* mutation; iso, isogenic control 1 generated from P1. **A** Co-immunostaining for cleaved-Caspase-3 (cCAS3) and CHAT in control, mutant and isogenic cultures. **B** Quantification experiments as in A. Data from 3 independent experiments per line were quantified. **C** Representative kinetics graphs of mitochondrial oxygen consumption rate. Quantification of maximum respiration (**D**) and spare respiratory capacity (**E**). Raw data from 3 independent experiments and at least 3 replicates per line were quantified. **F, G** Co-immunostaining for CHAT, DAPI and γ H2AX, a marker of the DNA damage response, after 1 h of neocarzinostatin (NCS) treatment. **G** Quantification of γ H2AX staining intensity in MN nuclei after NCS treatment. Data from 3 independent experiments per line were quantified. Results of three independent experiments are plotted as means with SEM * $p < 0.05$; **** $p < 0.0001$. **B, D, E, G** Kruskal–Wallis test, Dunn's multiple comparison post-hoc test. Scale bars: **A**, 100 μ m; **F**, 5 μ m

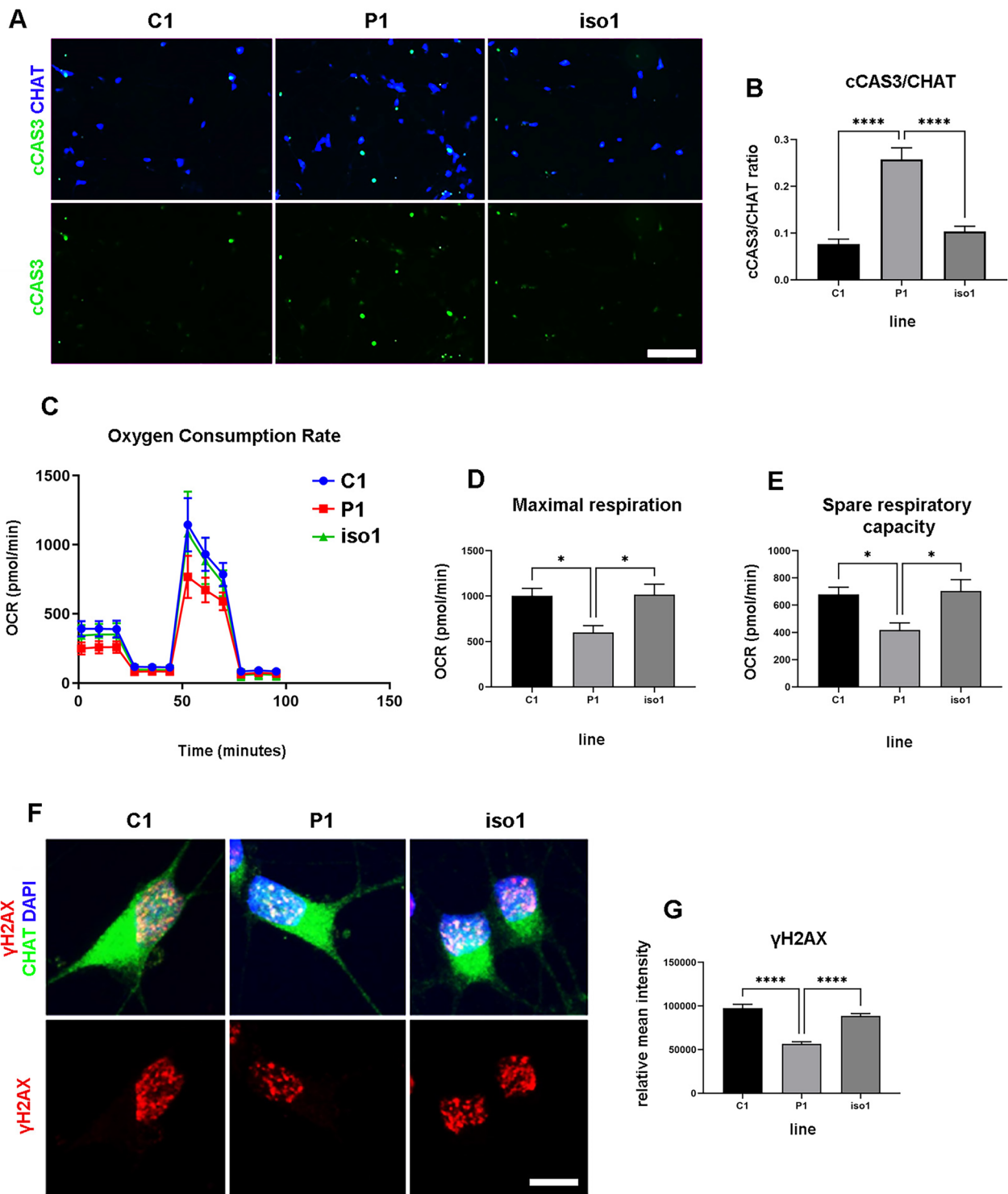


Fig. 5 (See legend on previous page.)

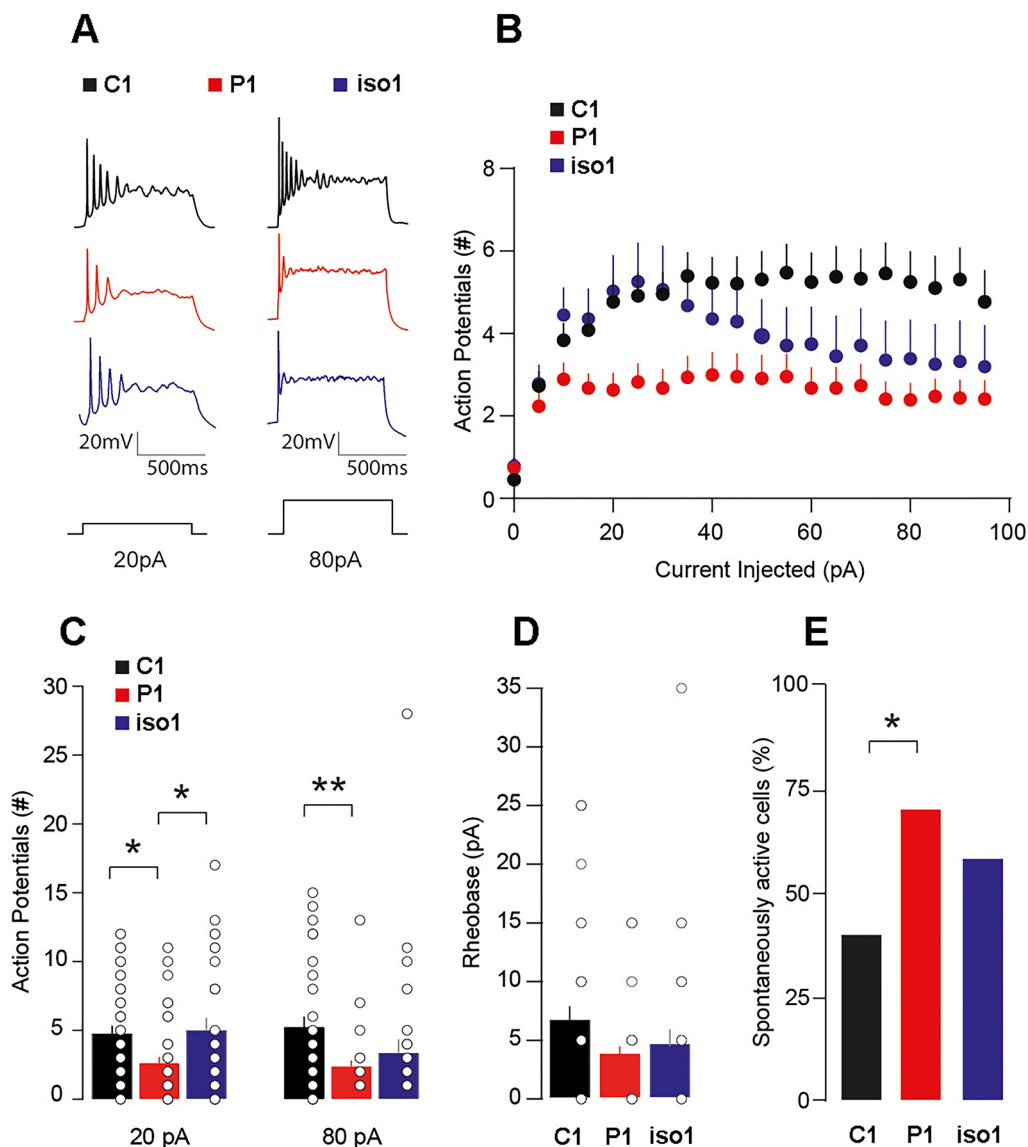


Fig. 6 Higher spontaneous activity but lower capacity for further stimulation-driven excitability in C21ORF2-V58L motor neurons. **A** Representative voltage traces in response to 20 pA or 80 pA depolarizing current injections across the three conditions: Healthy control 1 (C1, black), C21ORF2-V58L patient 1 (P1, red), and isogenic control 1 of P1 (iso1, blue). **B** Average current-action potential relationships in the three conditions: C1 (black; $n_{\text{cells}}=48$), P1 cells (red; $n_{\text{cells}}=46$), iso1 (blue; $n_{\text{cells}}=31$). Two-Way Repeated Measures ANOVA. Current \times Genotype interaction. $F(38,2318)=2.082$, $p=0.0001$. **C** Left: Bar graph with mean and SEM for action potential number in response to 20 pA across the three conditions. One-Way ANOVA: $F(2,122)=5.148$, $p=0.0071$. Tukey post-hoc tests. C1 versus P1, $p=0.0192$. C1 versus Iso1, $p=0.9517$; P1 versus Iso1, $p=0.0197$. Right: Same but in response to 80 pA. One-Way ANOVA: $F(2,122)=4.926$, $p=0.0088$. Tukey post-hoc tests. C1 versus P1, $p=0.0068$. C1 versus Iso1, $p=0.1712$; P1 versus Iso1, $p=0.6045$. **D** Bar graph plotted as means with SEM for rheobase across the three conditions. One-Way ANOVA: $F(2,122)=2.317$, $p=0.1029$. **E** Bar graphs with the percentage of spontaneously active cells at 0 pA injection steps across the three conditions. C1: 19/48 cells = 40%; P1: 32/46 cells = 70%; Iso1: 18/31 cells = 58%. Kruskal Wallis test = 8.606, $p=0.0135$. Dunn's post-hoc tests. C1 versus P1, $p=0.0108$; C1 versus Iso1, $p=0.3245$; P1 versus Iso1, $p=0.9647$. * $p < 0.05$; ** $p < 0.01$

that dysregulation of C21ORF2 by overexpression can lead to significant developmental defects, in line with the reported role of C21ORF2 in ciliopathies [28, 29, 31, 60]. To examine motor behaviour and MN connectivity, only embryos that did not show overt developmental defects

and were able to swim were included. Motor behaviour was assessed using the ZebraBox system (www.viewpoint.fr). Embryos were imaged for 1 h at 5 days post fertilization (5 dpf). This analysis showed a decrease in the duration and distance of swimming for zebrafish

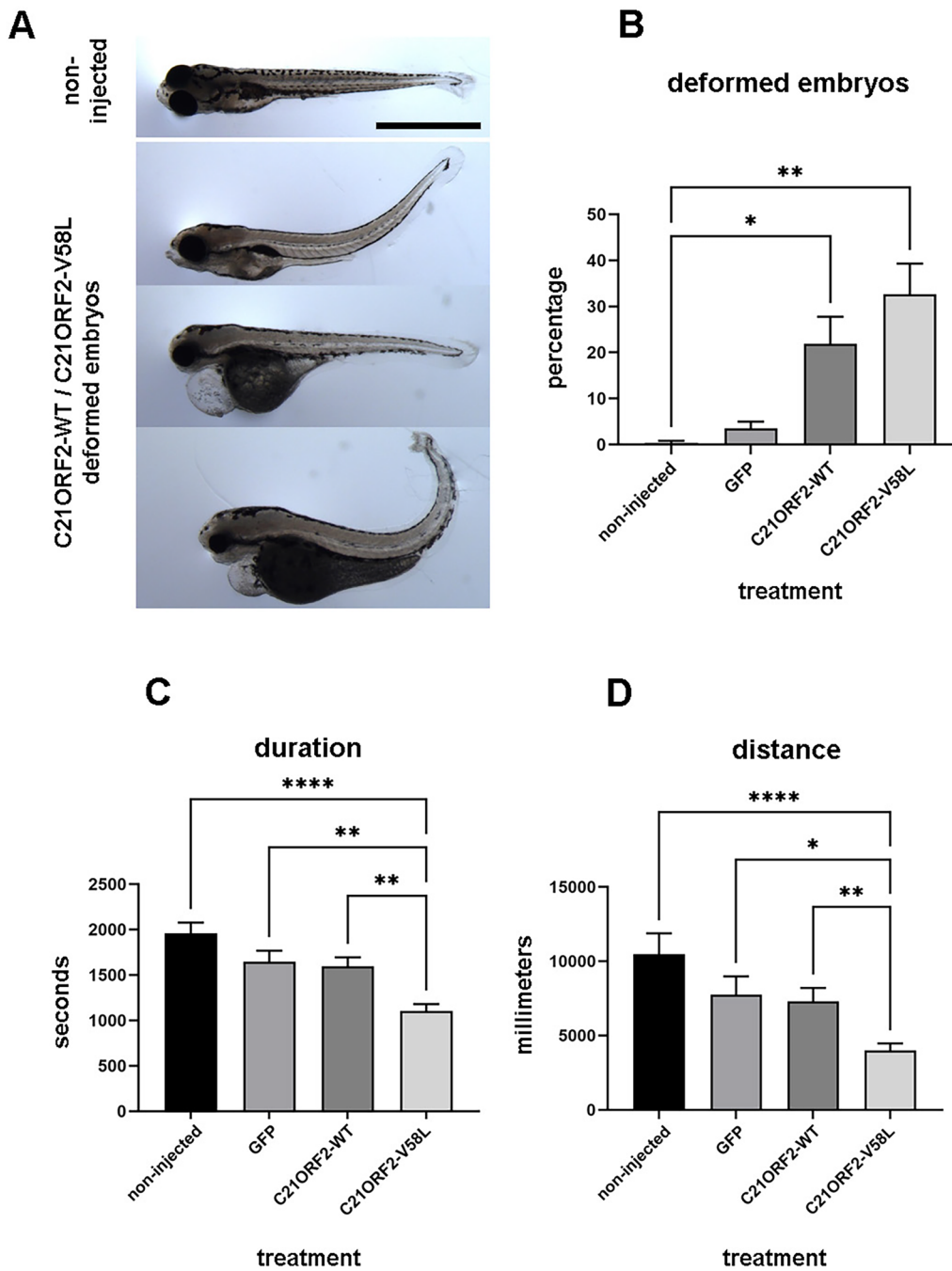


Fig. 7 C21ORF2-V58L impairs motor behavior in zebrafish embryos. **A** Representative images of 5 days post-fertilization (5 dpf) zebrafish embryos non-injected and injected with C21ORF2-WT or C21ORF2-V58L constructs. **B** Quantification of the number of deformed 5 dpf zebrafish embryos as in A. Pooled percentages from five independent experiments (total numbers of embryos analyzed—281 non injected embryos, 77 GFP injected embryos, 113 C21ORF2-WT injected embryos, 82 C21ORF2-V58L embryos). Data are shown as means with SEM $*p < 0.05$, $**p < 0.01$ Kruskal–Wallis test, Dunn’s multiple comparison post-hoc. **C, D** Zebrabox analysis of zebrafish embryo motor behavior at 5 dpf. Time spent swimming (seconds) and trajectory covered (millimeters) during 1 h were quantified. Pooled data from 4 independent experiments are plotted as means with SEM $*p < 0.05$, $**p < 0.01$, $****p < 0.0001$ Kruskal–Wallis test with Dunn’s multiple comparison post-hoc test. Scale bar: A, 1 mm

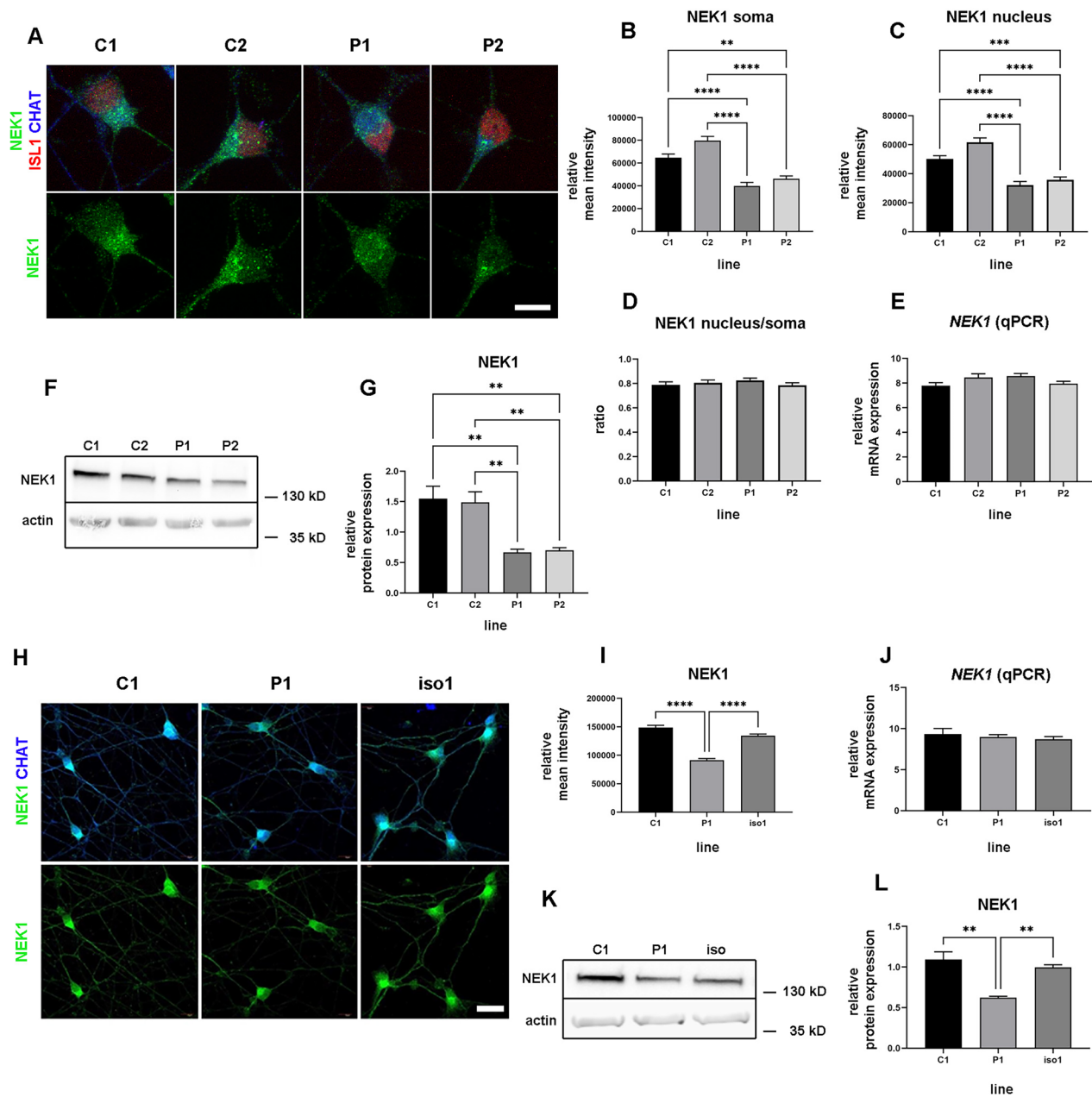


Fig. 8 C21ORF2-V58L affects NEK1 expression at the post-transcriptional level. **A–L** Analysis of NEK1 distribution and expression in iPSC-derived motor neuron (MN) cultures at days in vitro 25 (DIV25, 7 days after plating). C1 and C2, healthy controls; P1, ALS patient with C21ORF2-V58L mutation; P2, ALS patient with C21ORF2-V58L/R60W mutations; iso, isogenic control 1 generated from P1. **A** Co-immunostaining for NEK1 and CHAT/ISL1 to label MNs. **B, C** Quantification of NEK1 expression in soma and nucleus compartments based on immunostaining as in **A**. **D** Ratio of NEK1 immunostaining in nucleus compared to soma. **E** RT-q-PCR analysis of *NEK1* gene expression. For relative mRNA expression the $\Delta\Delta Ct$ values ($\Delta\Delta Ct = Ct(NEK1) - Ct(ACTINB)$) for each line are graphed. **F, G** Western blot analysis using anti-NEK1 and anti- β -actin antibodies. β -actin was used as loading control. **F** Representative Western blot. **G** Quantification of NEK1/actin intensity ratio in Western blot experiments as in **F**. **H–L** Immunostaining (**H, I**), RT-q-PCR (**J**), Western blot analysis (**K, L**) and corresponding quantifications using MNs derived from the C1, P1 and iso1 lines and performed as described for panels **A–G**. Results of three independent experiments are plotted as means with SEM ****** $p < 0.01$; ******* $p < 0.001$; ******** $p < 0.0001$, (G, L) One-Way ANOVA, Tukey multiple comparison post-hoc test. (**B, C, I**) Kruskal–Wallis test with Dunn’s multiple comparison post-hoc test. Scale bars: A, 5 μ m; I, 20 μ m

microinjected with C21ORF2-V58L mRNA as compared to GFP- or GFP-C21ORF2-WT-injected embryos (Fig. 7C, D). Defects in motor behaviour in zebrafish embryos caused by ALS mutant proteins can result from changes in the neuromuscular junction (NMJ) [16, 61–63]. Therefore, the NMJ was assessed at 5 dpf by immunostaining for synaptic vesicle protein 2 (SV2), a presynaptic marker, and labelling with α -bungarotoxin, a postsynaptic marker. However, no significant differences in the expression of or overlap between (as a measure of NMJ integrity) SV2 and α -bungarotoxin were found (Supplementary material 7: Supplementary Fig. S7F-J). Overall, these results suggest that the C21ORF2-V58L mutation affects motor behaviour in 5 dpf zebrafish embryos independent of overt changes in NMJ structure.

NEK1 expression is decreased in C21ORF2-V58L motor neurons and rescued by proteasomal inhibition

To begin to understand the molecular consequences of the C21ORF2-V58L mutation that lead to the observed cellular defects, the expression of several ALS-related proteins (i.e. those used as baits in our interactome experiments) was examined in control and patient MNs (Fig. 8A; Supplementary material 8: Supplementary Fig. S8A-J). The expression and distribution of most of these proteins appeared grossly normal (Supplementary material 8: Supplementary Fig. S8A-J), with the exception of NEK1 which showed reduced expression in C21ORF2-V58L MNs as visualized by immunocytochemistry (Fig. 8A). NEK1 expression was similarly reduced in both the cytoplasm and nucleus of mutant MNs (Fig. 8A-C).

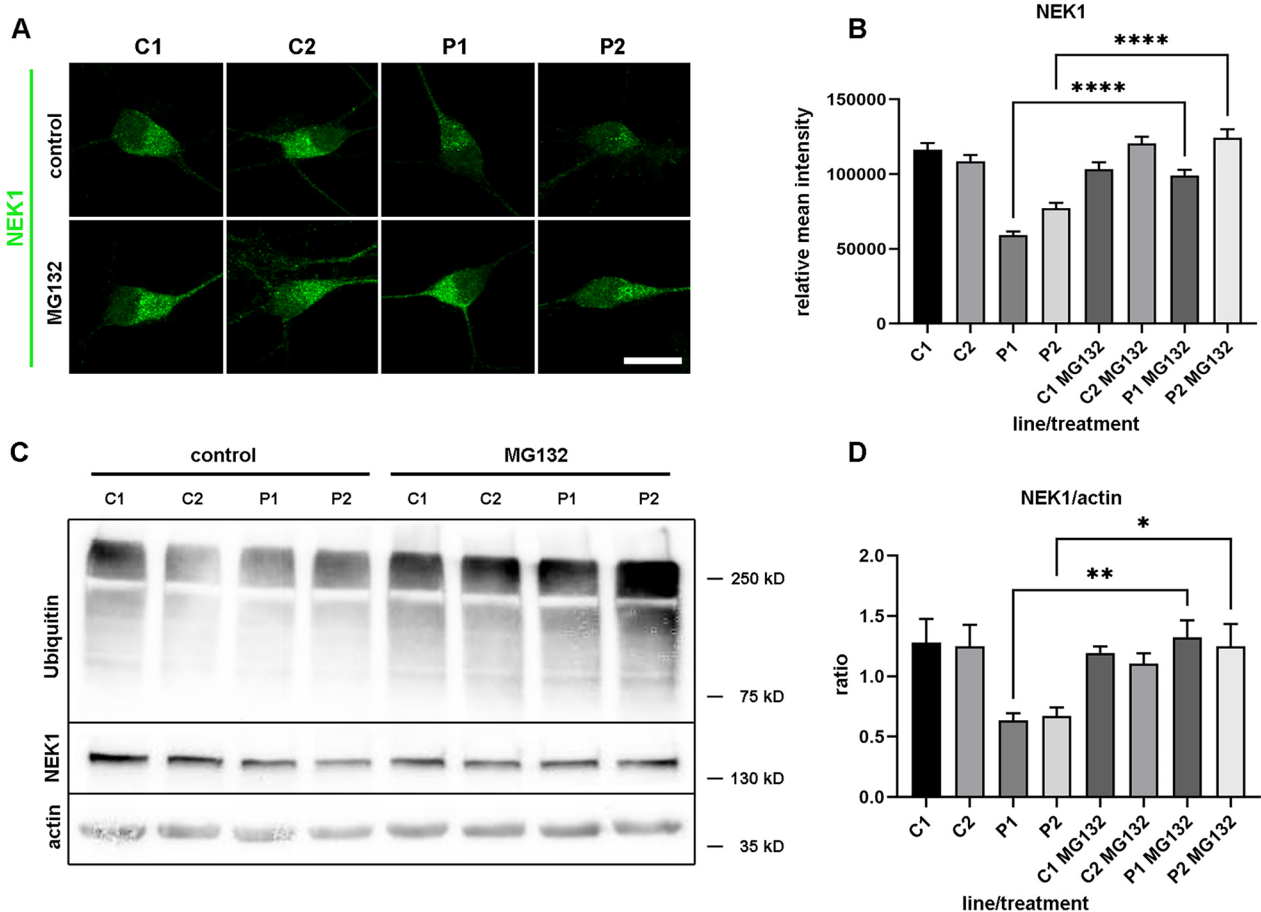


Fig. 9 Proteasomal inhibition reverses NEK1 downregulation in C21ORF2-V58L motor neurons. **A** Immunocytochemistry for NEK1 in MNs from two control (C1, C2) lines and two ALS patient lines carrying C21ORF2 mutations (P1, P2) treated with the proteasome inhibitor MG132 (100 nM, 3 h) or non-treated at days in vitro 7 (DIV7). **B** Quantification of immunostaining of NEK1 in control and mutant neurons without or with treatment with MG132 as in **A**. **C-D** Western blot analysis of lysates of control and mutant MNs without or with MG132 treatment. Western blot analysis using anti-ubiquitin, anti-NEK1 and anti- β -actin antibodies. Beta-actin was used as loading control. **C** Representative Western blot. **D** Quantification of Western blot experiments as in **C**. Results of 3 (**A, B**) and 5 (**C, D**) independent experiments are plotted as means with SEM * $p < 0.05$; ** $p < 0.01$; **** $p < 0.0001$. (B) Kruskal–Wallis test with Dunn’s multiple comparison post-hoc test. (D) One-Way ANOVA, Tukey multiple comparison post-hoc test. Scale bar: A, 10 μ m

The overall subcellular distribution of NEK1 was not changed (Fig. 8D), suggesting that transport of NEK1 between the cytoplasm and nucleus was not affected. Furthermore, while NEK1 mRNA expression was unchanged in C21ORF2-V58L MNs (Fig. 8E), Western blot analysis confirmed downregulation of NEK1 at the protein level (Fig. 8F, G). Immunocytochemistry, Western blot and qPCR analysis showed similar NEK1 expression in healthy and isogenic control MNs (Fig. 8H-L). To confirm this observation using a different experimental approach, C21ORF2-WT and -V58L were expressed in N2a neuronal cells followed by NEK1 immunostaining. In the line of our results in iPSC-derived MNs, endogenous NEK1 was significantly decreased in N2a cells expressing C21ORF2-V58L as compared to WT protein (Supplementary material 9: Supplementary Fig. S9A, B). Together, these data indicate that the C21ORF2-V58L mutation causes downregulation of NEK1 expression at the post-transcriptional level.

Next, we examined the neural expression pattern of NEK1 in more detail. Similar to C21ORF2, NEK1 was expressed in ALS relevant cell types, such as CTIP2-positive deep layer MNs in the mouse cortex and CHAT-positive MNs in the spinal cord (Supplementary material 9: Supplementary Fig. S9C). Co-expression analysis of NEK1 and C21ORF2 in N2a neuronal cells or mouse spinal MNs showed a granular distribution for both proteins and confirmed their co-localization (Supplementary material 9: Supplementary Fig. S9D, E). In line with these co-localization results, our interactome analysis and previous work showed that C21ORF2 and NEK1 can form a protein complex (Fig. 2G; Supplementary material 13: Supplementary Table S4B) [52]. To examine whether the C21ORF2-V58L mutation influences C21ORF2-NEK1 binding, co-immunoprecipitation using an anti-C21ORF2 antibody was performed on cell lysates from iPSC-derived MNs. NEK1 binding to C21ORF2-V58L was stronger as compared to wild-type C21ORF2 protein (Supplementary material 9: Supplementary Fig. 9F, G). Thus, the C21ORF2-V58L mutation influences NEK1 binding and expression.

As our results indicated that C21ORF2-V58L mutant protein causes a decrease in NEK1 protein at the post-transcriptional level, we explored a role for proteasomal degradation. iPSC-derived MNs were treated for 3 h with 100 nM of the proteasome inhibitor MG132 followed by analysis of NEK1 expression by immunostaining and Western blot analysis (Fig. 9A-D). MG132 treatment led to an accumulation of ubiquitinated protein that was not degraded by proteasome system. Interestingly, MG132 treatment reversed the decrease in NEK1 expression observed in C21ORF2-V58L MNs to control levels (Fig. 9A-D). This suggests that C21ORF2-V58L might

influence NEK1 protein expression by deregulating its proteasomal degradation.

Discussion

Genetic changes have been a valuable starting point for the dissection of ALS disease mechanisms. However, the contribution of many ALS-associated genetic mutations, and their effects at the protein level, remains poorly understood. Therefore, in this study the interactomes of five proteins recently linked to ALS, i.e. C21ORF2, KIF5A, NEK1, TBK1 and TUBA4A, were determined. The interactome experiments highlighted C21ORF2 as an important interaction hub participating in several molecular and cellular pathways. Subsequent studies of the ALS-associated C21ORF2-V58L variant showed various defects in zebrafish embryos *in vivo* and human iPSC-derived MNs *in vitro*. C21ORF2-V58L also induced decreased expression of another ALS-associated protein, NEK1, downregulation of which is connected to several of the phenotypes observed in C21ORF2-V58L MNs. Together, these results define the contribution of C21ORF2 to ALS pathogenesis and identify this gene as a potential interesting therapeutic target.

Common pathways downstream of ALS-associated proteins

In the present study, we expanded on our previous interactome analyses of FUS, TDP-43, C9ORF72, ATXN2, UBQLN2 and OPTN [16] by adding 5 more recently identified ALS-associated proteins: C21ORF2, KIF5A, NEK1, TBK1, and TUBA4A. The interactomes of these 11 ALS-associated proteins can help to identify underlying disease mechanisms in specific subsets of patients but also shared pathways that could aid the development of treatments aimed at larger groups of ALS patients. While our previous work identified a high degree of overlap between the interactomes of 1) ATXN2, FUS and TDP-43 and 2) OPTN and UBQLN2, our current data show shared interactors between C21ORF2, TBK1 and TUBA4A. Many of these interactors have chaperone functions, suggesting a shared contribution to protein quality control. This is in line with the implication of other ALS-associated proteins in the regulation of protein quality control, e.g. VCP, VAPBP, OPTN, UBQLN2, and SQSTM1 [64–68] and the link between heat-shock proteins, such as DNAJC7 (found in interactomes of both C21ORF2 and TUBA4A) and ALS [69]. It also supports the idea of targeting chaperone proteins as a treatment for ALS [70, 71]. The possibility that enrichment for chaperones in our proteomics data is due to overexpression of the bait proteins seems unlikely as chaperones are lacking in many interactomes, including those of aggregation-prone proteins such as TDP-43, FUS, and

SOD1 [72–78]. The specificity of our findings is further supported by the observation that most interactomes are rather specific. For example, while in our study the number of interactors for C21ORF2 and FUS is similar, their nature and reported functions are rather distinct. For example, FUS interactors play prominent roles in RNA/DNA metabolism, while the C21ORF2 interactome includes a variety of proteins linked to cytoskeletal regulation, chaperone function, and ribosomal and mitochondrial roles.

In addition to chaperone proteins, several other classes of proteins with relevant functions were shared between interactomes. For example, 14–3–3 proteins were enriched among the shared interactors of C21ORF2 and NEK1. 14–3–3 proteins are highly conserved regulatory proteins with strong neural expression and functions in diverse pathways such as membrane trafficking, apoptosis and neurite growth. Five 14–3–3 proteins that bind C21ORF2 and NEK1 also interact with OPTN and UBQLN2, while 2 shared 14–3–3 proteins were detected in the TBK1 interactome. Vice versa, no 14–3–3 proteins were identified in the interactomes of KIF5A, TUBA4A and FUS. 14–3–3 proteins have previously been implicated in the pathogenesis of different neurodegenerative disorders, including ALS [79]. For example, YWHAH colocalizes with TDP-43 granules in spinal cord tissue of sporadic ALS patients and YWHAQ promotes the cytoplasmic localization of TDP-43, while YWHAH and YWHAQ are trapped in mutant SOD1 aggregates in mice [80–82]. The relative abundance of 14–3–3 proteins in the interactomes of several ALS-associated proteins hints at a general role for these regulatory proteins in ALS pathogenesis. This is interesting as the recent development of specific tools to target 14–3–3 proteins begins to provide opportunities to interfere with their function in the context of disease [79, 82].

C21ORF2-V58L causes motor neuron phenotypes in vitro and in vivo

Our study showed that C21ORF2 shares a relatively high number of interactors with other ALS-associated proteins (NEK1, TBK1, TUBA4A) and hinted at several pathways downstream of C21ORF2 that are relevant for ALS pathogenesis (e.g. DNA damage repair, mitochondrial function and protein quality control). As C21ORF2 was a strongly connected protein and its neuronal functions in physiological and disease contexts largely unknown, we focused on C21ORF2 for more detailed analysis. Our data for the first time revealed C21ORF2 expression in mouse and human MNs, in line with a possible role in ALS pathogenesis, and showed that expression of an ALS-associated variant (C21ORF2-V58L) induces apoptosis in neurons. C21ORF2-V58L is the strongest

genetic risk variant within *C21ORF2* in ALS patients [17, 83] and is more susceptible to phosphorylation by NEK1 as compared to C21ORF2-WT in non-neuronal cells [51]. Therefore, this variant was selected for further studies in zebrafish embryos and human iPSC-derived MNs. It should be noted that the C21ORF2-V58L variant is also present in healthy controls in genome-wide association studies (GWAS), although at a much lower rate. This most likely reflects the importance of the remaining genetic background in patients and/or that C21ORF2-V58L expression represents a potential predisposition to ALS which will only fully appear later in life. Nevertheless, the generation and use of isogenic control iPSC lines allowed us to establish that most of the observed phenotypes are a consequence of the C21ORF2-V58L mutation.

The C21ORF2-V58L mutation localizes to the highly conserved leucine rich repeat (LRR) domain of C21ORF2 that mediates interactions with other proteins, e.g. NEK1 [52]. In line with this, we observed an increased interaction between C21ORF2-V58L and NEK1 in neurons, as compared to wild-type C21ORF2. It is therefore tempting to speculate that the V58L substitution alters the structural character of the LRR domain affecting its molecular interactions [84].

Overexpression of human C21ORF2 constructs (WT and V58L) in zebrafish embryos led to increased developmental deformation in part of the embryos, which may relate to the role of C21ORF2 in primary cilia [57]. In embryos that escaped these early and severe developmental defects and appeared morphologically normal, expression of C21ORF2-V58L, but not C21ORF2-WT, caused a decreased ability to swim, i.e. decreased motor function, in unhindered embryos. These defects were not caused by major structural changes at the neuromuscular junction (NMJ), although it is possible that C21ORF2-V58L affects NMJs at later, more mature stages. Given these observations, it is likely that behavioral defects at developmental stages are caused by molecular or functional changes in MNs or NMJs, for example those identified in iPSC-derived MNs carrying a C21ORF2-V58L mutation, especially at early disease stages (e.g. altered mitochondrial function or decreased excitability).

Regarding neuronal excitability profiles, we observed evidence for higher spontaneous activity in MNs (i.e. a form of hyperexcitability), but also evidence for less capacity to turn further stimulation into more action potentials (i.e. a form of hypo-excitability). Previous studies have also provided evidence for both hyper- and hypoexcitability in ALS models [85–87]. It has been proposed that hyperexcitability is the main hallmark of ALS MNs, and that, in so far as this takes the form of membrane depolarization, it results in inactivation of sodium currents and fewer action potentials upon further

stimulation (e.g. a depolarization block) [86]. The hyper-excitability phenotype was not rescued in isogenic control MNs, but hypo-excitability was decreased, at least following low levels of stimulation. This suggests that the mechanisms of hyper- and of hypo-excitability are at least partially dissociable in ALS MNs.

C21ORF2 has several reported functions, i.e. in cytoskeletal regulation, DNA repair and primary cilia formation and stability. Although C21ORF2 was first described in an exon trapping study aimed at identifying genes responsible for Down syndrome and other hereditary disorders [32], its functional role and mechanism-of-action in the nervous system were unknown. Our data show expression of C21ORF2 in different neuron types and reveal that an ALS-associated mutation in this protein affects reported or suggested functions of C21ORF2, i.e. in DDR and mitochondrial function, in human neurons. In previous work, immunostaining linked C21ORF2 to mitochondria [88], but no functional role had been established. Our data suggest that C21ORF2 is important for mitochondrial function as C21ORF2-V58L causes decreased mitochondrial metabolism in human MNs *in vitro*. In addition, C21ORF2 depletion in non-neuronal cells was shown to lead to impaired DNA damage repair [26]. In line with this, the DDR is reduced in MNs carrying the C21ORF2-V58L variant, suggesting this mutation may induce loss of C21ORF2 function in the context of the DDR. Interestingly, cross-talk exists between DDR or mitochondria and primary cilia [89, 90], and primary cilia are affected by knockout of and mutations in C21ORF2 [27, 29, 52, 91]. It is therefore possible that cilium defects act in line with an altered DDR or decreased mitochondrial metabolism in C21ORF2-ALS.

Our work also links (mutant) C21ORF2 to previously unexplored phenotypes and potential functions for this protein, such as apoptosis, neuronal excitability and motor behavior. Of several disease-associated C21ORF2 variants (ALS and/or ciliopathies) tested in our study, V58L induced increased apoptosis in primary neurons. This is intriguing as variants such as C21ORF2-L224P cause severe developmental ciliopathies (Jeune syndrome [27]), but no neuronal apoptosis in our *in vitro* experiments. It is plausible that the precise location of a mutation or its effect on protein structure determine its pathogenic effect. Further, the functional consequence or phenotypic expressivity of variants may also depend on cell type or other factors, such as the (epi)genetic background.

Together, these results provide insight into the role of C21ORF2 in healthy and diseased neurons and show that specific ALS-associated variants cause cellular and behavioral changes that have previously been linked to ALS. Further work is needed to assess whether the

observed phenotypes have a hierarchical relationship (e.g. defects in DDR or mitochondrial function leading to altered neuronal excitability and behavior and/or cell death) or act as independent disease mechanisms.

Decreased NEK1 levels in C21ORF2-V58L human motor neurons

C21ORF2 and NEK1 were the top hit in the interactome of the other protein, which is in line previous studies reporting prominent C21ORF2-NEK1 binding [27, 51, 52, 92]. C21ORF2 and NEK1 interactomes displayed considerable overlap, e.g. for 14–3–3 proteins. Further, of several ALS-associated proteins studied only NEK1 expression was visibly altered, at the protein but not mRNA level, in C21ORF2-V58L neurons. Similar to C21ORF2, NEK1 was localized to cortical and spinal cord MNs, and endogenous NEK1 binding was increased for C21ORF2-V58L as compared to C21ORF2-WT in human MNs. Reduced NEK1 expression has also been found following knock-out of C21ORF2 in HEK293, while upregulation of C21ORF2 in SH-SY5Y cells increased NEK1 expression [51]. In N2a cells, we find that ectopic expression of C21ORF2-V58L induces reduced NEK1 expression. Mechanistically, our data suggest that C21ORF2-V58L enhances NEK1 degradation, possibly via stronger binding. We were not able to detect significant ubiquitination of NEK1 in human MNs (unpublished observations), hinting at the potential involvement of ubiquitin-independent proteasome degradation or other mechanisms, such as lysosomal degradation. Previous studies had shown decreased C21ORF2-V58L-NEK1 binding, NEK1 accumulation and reduced mRNA expression, and altered C21ORF2-V58L levels when using protein over-expression in non-neuronal cells [51]. This suggests that the effects of C21ORF2-V58L on NEK1 are likely cell type-dependent and/or influenced by other factor such as (ectopic) protein levels or the presence of an ALS genetic background.

Several studies connect NEK1 loss or dysfunction with decreased DDR, mitochondria dysfunction and/or apoptosis in different cell types [34–36, 93–96]. Given our observation that C21ORF2-V58L causes reduced NEK1 levels in MNs it is tempting to speculate that some of phenotypes observed in C21ORF2-V58L neurons result from decreased NEK1 expression. As impaired DDR caused by C21ORF2 depletion could be rescued by over-expression of NEK1 [26], we attempted to re-express NEK1 in C21ORF2-V58L MNs to further establish the functional consequences of reduced NEK1. Unfortunately, both knockdown and overexpression of NEK1 in human MNs caused extensive cell death precluding analysis (unpublished observations). Therefore, further

studies are needed to study NEK1 deregulation in the context of ALS-associated C21ORF2 mutations in MNs.

Conclusions

In conclusion, our study reports a novel dataset composed of the interactomes of 5 ALS-associated proteins that provide a framework for future studies into the pathogenesis of ALS or other diseases linked to the proteins. We identify C21ORF2 as a highly connected protein. Functional studies show that the ALS-associated C21ORF2-V58L variant induces various ALS relevant defects in zebrafish embryos *in vivo* and human iPSC-derived MNs *in vitro*, including apoptosis, reduced motor behavior and decreased NEK1 expression. Thus, these results begin to define the role of C21ORF2 in ALS pathogenesis and identify the C21ORF2-NEK1 complex as an interesting therapeutic target in ALS.

Abbreviations

AA	Ascorbic acid
ABC	Ammonium bicarbonate
ACSF	Artificial cerebrospinal fluid
ALS	Amyotrophic lateral sclerosis
AP	Action potential
ATXN2	Ataxin-2
BDNF	Brain-derived neurotrophic factor
BTX	α -Bungarotoxin
C9ORF72	Chromosome 9 open reading frame 72
C21ORF2	Chromosome 21 open reading frame 2
C1, C2	Control 1, control 2
cAMP	Cyclic adenosine monophosphate
cCAS3	Cleaved caspase-3
CCD	Centrale Commissie Dierproeven
CEA	Chicken egg white
CFAP410	Cilia and flagella associated protein 410
CHAT	Choline acetyltransferase
CMT2	Charcot-Marie-Tooth disease type 2
CNTF	Ciliary neurotrophic factor
CRISPR	Clustered regularly interspaced short palindromic repeats
DAPI	4',6-Diamidino-2-phenylindole
DIV	Days in vitro
DDR	DNA damage response
fALS	Familial amyotrophic lateral sclerosis
FCCP	P-Trifluoromethoxyphenylhydrazone
FGF	Fibroblast growth factor
FMRP	Fragile X mental retardation protein
FUS	Fused in sarcoma
GDNF	Glial cell line-derived neurotrophic factor
GWAS	Genome-wide association study
huES	Human embryonic stem cell
iPSC	Induced pluripotent stem cells
Iso1	Isogenic control 1
KIF5A	Kinesin family member 5A
LRR	Leucine rich repeat
MN	Motor neurons
N2a	Neuro-2a cells
NDM	Neuronal differentiation medium
NEAA	Non-essential amino acids
NEK1	NIMA-related kinase 1
NMJ	Neuro-muscular junction
PBS	Phosphate buffered saline
PBSGT	PBS + 0.2% gelatin + 0.5% Triton X-100
PDL	Poly-D-lysine
PFA	Paraformaldehyde

NCS	Neocarzinostatin
NDS	Normal donkey serum
NEAA	Non-essential amino acids
OCR	Oxygen consumption rate
ON	Overnight
OPTN	Optineurin
P1, P2	Patient 1, patient 2
RA	Retinoic acid
ROCK	Rho-associated protein kinase
RT	Room temperature
RT-qPCR	Reverse transcription quantitative polymerase chain reaction
sALS	Sporadic amyotrophic lateral sclerosis
SPG10	Spastic paraplegia-10
SV2	Synaptic vesicle protein 2
TBK1	TANK-binding kinase 1
TBS	Tris-buffered saline
TBS-T	TBS + 0.01% Tween-20
TDP-43	TAR DNA-binding protein 43
TUBA4A	Tubulin alpha 4A
UBQLN2	Ubiquilin2
WT	Wild type

Supplementary Information

The online version contains supplementary material available at <https://doi.org/10.1186/s40478-024-01852-6>.

Supplementary material 1: Supplementary Fig. S1: Full Western blots of immunoprecipitated GFP-tagged proteins. (A-F) Constructs encoding GFP or GFP-tagged (bait) proteins were expressed in Neuro2a cells followed by pull-down with GFP-Trap beads and Western blot analysis. All 6 GFP-tagged bait proteins were expressed at the expected molecular weight and enriched in the pull-down sample.

Supplementary material 2: Supplementary Fig. S2: Shared interactors of C21ORF2-TBK1-TUBA4A and C21ORF2-NEK1. (A, B) Venn diagrams showing the number of unique and overlapping interactors of C21ORF2, TUBA4A and TBK1 (A), and NEK1 and C21ORF2 (B). (C, D) Network plot of known interactions between shared interactors of C21ORF2, TUBA4A and TBK1 (C), and NEK1 and C21ORF2 (D).

Supplementary material 3: Supplementary Fig. S3: Expression of C21ORF2 and C21ORF2 mutant variants. (A) GFP-tagged full length C21ORF2 or deletion mutants were expressed in N2a cells. The longest human C21ORF2 isoform (NM_001271441.1) was used and an N-terminal GFP-tag was added. aa, amino acid. (B) Protein structure prediction software (<http://raptorx6.uchicago.edu>) predicts three major domains (NP_001258370): aa 1-142 (N-terminal domain), aa 143-213 (middle low complexity domain) and aa 214-376 (C-terminal domain). (C) Analysis of the human C21ORF2 sequence (NP_001258370) identifies an N-terminal nuclear localization signal (NLS in red according to cNLS (https://nls-mapper.iab.keio.ac.jp/cgi-bin/NLS_Mapper_form.cgi) and a C-terminal nuclear export signal (NES in blue according to LocNES (<http://proddata.swmed.edu/LocNES/LocNES.php>)). (D) Co-immunohistochemistry for TUJ1 and GFP followed by confocal microscopy showing expression of GFP, wild type GFP-tagged C21ORF2 (C21ORF2-WT) or GFP-tagged C21ORF2 variants in mouse primary cortical neurons at days in vitro (DIV) 5. Scale bars: A, D, 10 μ m.

Supplementary material 4: Supplementary Fig. S4: Characterization of iPSC lines and motor neuron differentiation. iPSC cells were created from fibroblasts (cultured from human skin biopsies) using the CytoTune-iPS 2.0 Sendai Reprogramming Kit (Invitrogen). Two control lines, C1 (clone C13), C2 (clone PZ1-5), and 2 ALS patient lines, P1 (clone A14) and P2 (clone 2216-6), were generated. (A) All iPSC lines displayed normal karyotypes. (B) Representative images of the expression of the pluripotency markers OCT-4A, SOX2, NANOG, SSEA4, TRA-1, TRA-1-81. Expression was examined in all lines by immunostaining using the StemLight™ Pluripotency Antibody Kit – CST. (C) Quantitative RT-PCR for the pluripotency markers KLF4, C-MYC, NANOG, OCT4 and SOX2. 'Relative mRNA expression' is represented by $2^{-\Delta\Delta CT}$ values using the ACTIN gene as reference and compared to expression in human

embryonic stem cells (huES) as a control for expression of the relevant genes. (D) Representative images of the results of spontaneous differentiations using STEMdiff™ Trilineage Differentiation Kit - STEMCELL Technologies followed by staining for ectoderm (NESTIN), mesoderm (NCAM, BRACHYURY) and endoderm (CXCR4) markers. (E) Schematic representation of the motor neuron differentiation protocol used (modified from Du et al., 2015). At day 25 of differentiation (DIV25, 7 days after plating), neurons expressed the motor neuron markers CHAT and ISL1. Scale bars: B, 5 µm; D, 10 µm; E, D0-D18 200 µm; D25 20 µm.

Supplementary material 5: Supplementary Fig. S5: Morphological analysis of C21ORF2-V58L motor neurons. (A-C) C1 and C2, healthy controls; P1, ALS patient with C21ORF2-V58L mutation; P2, ALS patient with C21ORF2-V58L/R60W mutations. Quantification of the size of the neuronal cell body and nucleus of control and mutant motor neurons (MNs), and the corresponding nucleus/soma ratio at days in vitro 25 (DIV25, 7 days after plating). (D) Immunohistochemistry for tubulin (TUJ1) in DIV21 (3 days after plating) control and mutant iPSC-derived MNs. (E-G) Quantification of total neurite length, length of the main (longest) neurite (axon) and the number of branches of MNs. Results are plotted as means with SEM (A - C) Three independent experiments and at least 10 neurons analyzed per line. (E - G) Four independent experiments and at least 40 neurons analyzed per line. Scale bar: D, 50 µm.

Supplementary material 6: Supplementary Fig. S6: Generation and characterization of an isogenic control line. An isogenic line was generated from the P1 iPSC line (carrying a C21ORF2-V58L mutation) using a CRISPR/Cas9 approach. (A) Sequence analysis of P1 and the corresponding isogenic control (Iso1) created from P1 shows removal of the heterozygous G>T mutation. (B) The isogenic control line (Iso1) displayed a normal karyotype. (C) Quantitative RT/q-PCR for the pluripotency markers KLF4, C-MYC, NANOG, OCT4 and SOX2. Relative mRNA expression is represented by $2^{-\Delta\Delta Ct}$ values using ACTIN gene as reference and compared to expression in human embryonic stem cells (huES) as a control for expression of the relevant genes. (D) Co-immunocytochemistry for C21ORF2 and CHAT in iPSC-derived MNs at days in vitro 25 (DIV25, 7 days after plating). (E) Quantification of immunostainings as in D. (F) Quantitative RT/q-PCR analysis of C21ORF2 gene expression in control, iso1 and mutant MNs at DIV25. For relative mRNA expression the ΔCt values ($\Delta Ct = Ct(C21ORF2) - Ct(ACTINB)$) for each line are shown. (G) Western blot analysis at DIV25 using anti-C21ORF2 and anti-actin antibodies. actin was used as loading control. (H) Quantification of C21ORF2/actin intensity ratio in Western blot experiments as in G. Results of at least three independent experiments are plotted as means with SEM. Scale bar: D, 50 µm.

Supplementary material 7: Supplementary Fig. S7: Electrophysiological examination of C21ORF2-V58L motor neurons and synaptic analysis in zebrafish embryos. (A) Top: Brightfield image of a representative cell culture. Bottom: Example of a biocytin filled patched motor neuron. C2, healthy control; P2, ALS patient with C21ORF2-V58L/R60W mutations. (B) Average current-action potential relationship in cells obtained from C2 (gray; ncells=33) and P2 (red; ncells=17). Two-Way Repeated Measures ANOVA. Main effect of genotype; $F(1,48)=5.01$, $p=0.03$. (C) Action potentials elicited by 80 pA current injection. Unpaired t-test $t(48)=2.096$, $p=0.0414$. (D) Bar graph plotted as means with SEM for rheobase across the two conditions. Unpaired t-test $t(49)=2.224$, $p=0.0308$. (E) Bar graphs with the percentage of spontaneously active cells at 0 pA injection steps across the two conditions. C2: 7/33 cells=21%; P2: 12/19 cells=63%. Mann Whitney U test = 182, $p=0.0035$. * $p<0.05$; ** $p<0.01$. (F - J) Zebrafish embryos were injected with mRNA for GFP, wild type C21ORF2 (WT) or C21ORF2-V58L (V58L). Embryos were collected 5 days post fertilisation (dpf) and immunostained for synaptic vesicle protein 2 (SV2), as a presynaptic marker, and with α -bungarotoxin (BTX), as a postsynaptic marker. Z-stack confocal images of the ventral portion of the zebrafish embryo corresponding to the 17th-18th somite were obtained and analyzed. Boxed area is

shown at higher magnification at the right. (G, H) SV2 and BTX staining intensity analyzes using Fiji software for four conditions. (I) Ratio of BTX to SV2 staining. (J) Imaris software was used to analyse the immunostaining of embryos in 3D. Colocalization between SV2 and BTX was calculated in Imaris with the function "spots close to surface". BTX signal was transformed into "spots", while SV2 signal was transformed into "surfaces" (last two right panels in F). The percentage of BTX "spots" within a determined distance (0.05 µm) from the SV2 "surface" was quantified. Scale bar: A upper panel 10 µm, lower panel 100 µm; F low magnification 20 µm, high resolution (last right panel) 5 µm.

Supplementary material 8: Supplementary Fig. S8: Expression and distribution of ALS-associated proteins in C21ORF2-V58L motor neurons. (A-J) Expression analysis of iPSC-derived motor neuron (MN) in DIV25 (7 days after plating) cultures. C1 and C2, healthy controls; P1, ALS patient with C21ORF2V58L mutation; P2, ALS patient with C21ORF2-V58L/R60W mutations. Co-immunostaining of CHAT (to label MNs) and different ALS-associated proteins that were analysed in our current and previous interatomic studies. (A) ATX2, (B) C9ORF72, (C) FUS, (D) KIF5A, (E) OPTN, (F) SOD1, (G) TBK1, (H) TDP-43, (I) TUBA4A, (J) UBQLN. Scale bar: A-J, 10 µm.

Supplementary material 9: Supplementary Fig. S9: Expression of NEK1 and interaction with C21ORF2. (A) Immunostaining for NEK1 in Neuro2a (N2a) cells (non-transfected, or transfected with constructs for GFP, GFP-tagged C21ORF2-WT or GFP-tagged C21ORF2-V58L). (B) Quantification of NEK1 immunostaining as in A. Results of three independent experiments with 10 optical fields quantified per condition are plotted as means with SEM. *** $p<0.001$; **** $p<0.0001$. Kruskal-Wallis test with Dunn's multiple comparison post-hoc test. (C) Coronal sections of adult mouse motor cortex (upper panels) and spinal cord (lower panels) were co-immunostained for NEK1 and CTIP2 (upper panels) or CHAT (lower panels) to mark upper and lower MNs, respectively. Squares in left panels are shown at higher magnification in the right three panels. (D, E) Co-immunostaining of endogenous C21ORF2 and NEK1 in cultured N2a cells (D) and in vivo in adult mouse spinal cord motor neurons (E). C21ORF2 and NEK1 show overlapping staining (D) and similar localization (arrows in E). (F, G) Immunoprecipitation of endogenous C21ORF2 protein from lysates of C1 and P1 iPSC-derived MNs at days in vitro 25 (DIV25, 7 days after plating). Although both C21ORF2 and C21ORF2-V58L pull-down NEK1 protein, the interaction between NEK1 and C21ORF2-V58L appears stronger as shown by quantification of Western blots from 3 independent experiments (plotted as means with SEM) (G). * $p<0.05$; unpaired t-test. Scale bars: A, 50 µm; C, 200 µm (low magnification), 20 µm (high magnification); D 10 µm; E, 10 µm.

Supplementary material 10: Supplementary Table S1 A-C: Interaction partners of FUS protein.

Supplementary material 11: Supplementary Table S2 A-E: Interaction partners of C21ORF2, KIF5A, NEK1, TBK1 and TUBA4A.

Supplementary material 12: Supplementary Table S3 A-F: GO analysis of interactors of C21ORF2, FUS, KIF5A, NEK1, TBK1 and TUBA4A.

Supplementary material 13: Supplementary Table S4 A-B: Shared interactors of C21ORF2-TBK1-TUBA4A and C21ORF2-NEK1.

Supplementary material 14: Supplementary Table S5: C21ORF2 mutant variants for expression constructs.

Supplementary material 15: Supplementary Table S6: Clinical data ALS patients and healthy controls.

Supplementary material 16: Supplementary Table S7: Biophysical membrane parameters across experimental conditions.

Acknowledgements

We thank Jeroen den Hertog, Niels Geijsen, Alain Chedotal, Nilo Riva, Dario Bonanomi, and Casper Hoogenraad for providing reagents and advice. We thank Renata Vieira de Sá, Sandra Kling, Danielle Vonk, Lauri Bloemenkamp, Ewout Groen, Mark H. Broekhoven, Nicky van Kronenburg, Youri Adolf, Bram Schipper, Maria Celeste Cantone, Nick Papavoine, Pascale Dijkers, Miranda van Triest, Bobby Koeleman, Sanne Savelberg, Robert M. van Es, Paula Sobrevalls

Alcaraz, Sabine van Doeselaar, Mark Reijnen and Maaike Allers for help and technical support.

Author contributions

Conceptualization, P.Z., A.A.D.R., R.J.P.; methodology, P.Z., A.A.D.R., H.R.V., R.J.P.; experimental studies, P.Z., A.A.D.R., C.K., I.G., H.R.V., L.F.S.; clinical data & patient material, J.H.V., L.H.B.; writing—original draft, P.Z., A.A.D.R., R.J.P.; writing—review, all; supervision, R.J.P.; funding acquisition, R.J.P.

Funding

This project was financially supported by Stichting ALS Nederland (TOTALS, GoALS), the MAXOMOD consortium (E-Rare-3, the ERANet for Research on Rare Diseases), ALS CURE project, and the EU joint Program Neurodegenerative Diseases (JPN-D; TRIAGE) (to R.J.P.) and the X-omics initiative (NWO, project 184.034.019 to B.M.T.B.). This project has received funding from the European Research Council (ERC) under the European Union's Horizon 2020 research and innovation programme (grant agreement n° 772376—EScORIAL).

Availability of data and materials

Proteomics data is deposited at: <http://www.ebi.ac.uk/pride>. Project Name: Comparative interactome analyses of ALS proteins help define the pathogenic effects of mutant C21ORF2 in motor neurons. Project accession: PXD051922.

Declarations

Ethics approval and consent to participate

All subjects have provided written informed consent and generation of iPSC lines was approved by the Ethical Medical Committee of the University Medical Center Utrecht. Patients were diagnosed according to the diagnostic criteria for ALS (revised El Escorial). Controls were donors without a psychiatric or neurologic diagnosis (Supplementary material 15: Supplementary Table S6).

Consent for publication

Not applicable.

Competing interests

J.H.V. reports to have sponsored research agreements with Biogen and Astra Zeneca. R.J.P. reports to have sponsored research agreements with Amylyx. The other authors declare no competing interests.

Author details

¹Department of Translational Neuroscience, University Medical Center Utrecht Brain Center, Utrecht University, Universiteitsweg 100, 3584 CG Utrecht, The Netherlands. ²Department of Neurology and Neurosurgery, UMC Utrecht Brain Center, University Medical Center Utrecht, Utrecht University, 3584 CX Utrecht, The Netherlands. ³Center for Molecular Medicine, Oncode Institute, University Medical Center Utrecht, Utrecht University, Universiteitsweg 100, 3584 CG Utrecht, The Netherlands.

Received: 11 July 2024 Accepted: 15 August 2024

Published online: 04 September 2024

References

- Brown RH, Al-Chalabi A (2017) Amyotrophic lateral sclerosis. *N Engl J Med* 377:162–172. <https://doi.org/10.1056/NEJMr1603471>
- Masrori P, Van Damme P (2020) Amyotrophic lateral sclerosis: a clinical review. *Eur J Neurol* 27:1918–1929. <https://doi.org/10.1111/ene.14393>
- Longinetti E, Fang F (2019) Epidemiology of amyotrophic lateral sclerosis: an update of recent literature. *Curr Opin Neurol* 32(5):771–776. <https://doi.org/10.1097/wco.0000000000000730>
- Al-Chalabi A, Hardiman O (2013) The epidemiology of ALS: a conspiracy of genes, environment and time. *Nat Rev Neurol* 9:617–628. <https://doi.org/10.1038/nrneurol.2013.203>
- Al-Chalabi A, Calvo A, Chio A, Colville S, Ellis CM, Hardiman O, Heverin M, Howard RS et al (2014) Analysis of amyotrophic lateral sclerosis as a multistep process: a population-based modelling study. *Lancet Neurol* 13:1108–1113. [https://doi.org/10.1016/S1474-4422\(14\)70219-4](https://doi.org/10.1016/S1474-4422(14)70219-4)
- Chia R, Chiò A, Traynor BJ (2018) Novel genes associated with amyotrophic lateral sclerosis: diagnostic and clinical implications. *Lancet Neurol* 17:94–102. [https://doi.org/10.1016/S1474-4422\(17\)30401-5](https://doi.org/10.1016/S1474-4422(17)30401-5)
- Al-Chalabi A, Jones A, Troakes C, King A, Al-Sarraj S, Van Den Berg LH (2012) The genetics and neuropathology of amyotrophic lateral sclerosis. *Acta Neuropathol* 124:339–352
- Al-Chalabi A, van den Berg LH, Veldink J (2016) Gene discovery in amyotrophic lateral sclerosis: implications for clinical management. *Nat Rev Neurol* 13:96–104. <https://doi.org/10.1038/nrneurol.2016.182>
- Nguyen HP, Van Mossevelde S, Dillen L, De Bleecker JL, Moisse M, Van Damme P, Van Broeckhoven C, van der Zee J, BELNEU Consortium (2018) NEK1 genetic variability in a Belgian cohort of ALS and ALS-FTD patients. *Neurobiol Aging* 61:255.e1–255.e7. <https://doi.org/10.1016/j.neurobiolaging.2017.08.021>
- Zou ZY, Zhou ZR, Che CH, Liu CY, He RL, Huang HP (2017) Genetic epidemiology of amyotrophic lateral sclerosis: a systematic review and meta-analysis. *J Neurol Neurosurg Psych* 88:540–549. <https://doi.org/10.1136/jnnp-2016-315018>
- Van Damme P, Robberecht W, Van Den Bosch L (2017) Modelling amyotrophic lateral sclerosis: progress and possibilities. *DMM Disease Models Mech* 10:537–549. <https://doi.org/10.1242/dmm.029058>
- Balendra R, Isaacs AM (2018) C9orf72-mediated ALS and FTD: multiple pathways to disease. *Nat Rev Neurol* 14:544–558. <https://doi.org/10.1038/s41582-018-0047-2>
- Burk K, Pasterkamp RJ (2019) Disrupted neuronal trafficking in amyotrophic lateral sclerosis. *Acta Neuropathol* 137:859–877. <https://doi.org/10.1007/s00401-019-01964-7>
- Vahsen BF, Gray E, Thompson AG, Ansong O, Anthony DC, Cowley SA, Talbot K, Turner MR (2021) Non-neuronal cells in amyotrophic lateral sclerosis - from pathogenesis to biomarkers. *Nat Rev Neurol* 17:333–348. <https://doi.org/10.1038/s41582-021-00487-8>
- Groen EJ, Fumoto K, Blokhuis AM, Engelen-Lee J, Zhou Y, van den Heuvel DM, Koppers M et al (2013) ALS-associated mutations in FUS disrupt the axonal distribution and function of SMN. *Hum Mol Genet* 22:3690–3704. <https://doi.org/10.1093/hmg/ddt222>
- Blokhuis AM, Koppers M, Groen EJM, van den Heuvel DMA, Dini Modigliani S, Anink JJ, Fumoto K et al (2016) Comparative interactomics analysis of different ALS-associated proteins identifies converging molecular pathways. *Acta Neuropathol* 132:175–196. <https://doi.org/10.1007/s00401-016-1575-8>
- van Rheenen W, Shatunov A, Dekker AM, McLaughlin RL, Diekstra FP, Pulit SL, van der Spek RA et al (2016) Genome-wide association analyses identify new risk variants and the genetic architecture of amyotrophic lateral sclerosis. *Nat Genet* 48:1043–1048. <https://doi.org/10.1038/ng.3622>
- Brenner D, Yilmaz R, Müller K, Grehl T, Petri S, Meyer T, Grosskreutz J, Weydt P, Ruf W, Neuwirth C et al (2018) German ALS network MND-NET. Hot-spot KIF5A mutations cause familial ALS. *Brain* 141:688–697. <https://doi.org/10.1093/brain/awx370>
- Nicolas A, Kenna KP, Renton AE, Ticozzi N, Faghri F, Chia R, Dominov JA, Kenna BJ, Nalls MA et al (2018) Genome-wide analyses identify KIF5A as a novel ALS Gene. *Neuron* 97:1268–1283.e6. <https://doi.org/10.1016/j.neuron.2018.02.027>
- Brenner D, Müller K, Wieland T, Weydt P, Böhm S, Lulé D, Hübers A, Neuwirth C, Weber M et al (2016) NEK1 mutations in familial amyotrophic lateral sclerosis. *Brain* 139(Pt 5):e28. <https://doi.org/10.1093/brain/aww033>
- Kenna KP, van Doormaal PT, Dekker AM, Ticozzi N, Kenna BJ, Diekstra FP, van Rheenen W et al (2016) NEK1 variants confer susceptibility to amyotrophic lateral sclerosis. *Nat Genet* 48:1037–1042. <https://doi.org/10.1038/ng.3626>
- Cirulli ET, Lasseigne BN, Petrovski S, Sapp PC, Dion PA, Leblond CS, Couthouis J, Lu YF, Wang Q et al (2015) Exome sequencing in amyotrophic lateral sclerosis identifies risk genes and pathways. *Science* 347:1436–1441. <https://doi.org/10.1126/science.1256550>
- Freischmidt A, Wieland T, Richter B, Ruf W, Schaeffer V, Müller K, Marroquin N, Nordin F, Hübers A et al (2015) Haploinsufficiency of TBK1 causes familial ALS and fronto-temporal dementia. *Nat Neurosci* 18:631–636. <https://doi.org/10.1038/nn.4000>

24. Smith BN, Ticozzi N, Fallini C, Gkazi AS, Topp S, Kenna KP, Scotter EL, Kost J, Keagle P et al (2014) Exome-wide rare variant analysis identifies TUBA4A mutations associated with familial ALS. *Neuron* 84:324–331. <https://doi.org/10.1016/j.neuron.2014.09.027>
25. Bai SW, Herrera-Abreu MT, Rohn JL, Racine V, Tajadura V, Suryavanshi N, Bechtel S et al (2011) Identification and characterization of a set of conserved and new regulators of cytoskeletal organization, cell morphology and migration. *BMC Biol* 9:54. <https://doi.org/10.1186/1741-7007-9-54>
26. Fang X, Lin H, Wang X, Zuo Q, Qin J, Zhang P (2015) The NEK1 interactor, C21ORF2, is required for efficient DNA damage repair. *Acta Biochim Biophys Sin (Shanghai)* 47(10):834–841. <https://doi.org/10.1093/abbs/gmv076>
27. Wheway G, Schmidts M, Mans DA, Szymanska K, Nguyen TT, Racher H, Phelps IG, Toedt G et al (2015) An siRNA-based functional genomics screen for the identification of regulators of ciliogenesis and ciliopathy genes. *Nat Cell Biol* 17:1074–1087. <https://doi.org/10.1038/ncb3201>
28. Suga A, Mizota A, Kato M, Kuniyoshi K, Yoshitake K, Sultan W, Yamazaki M, Shimomura Y, Ikeo K, Tsunoda K, Iwata T (2016) Identification of novel mutations in the LRR-Cap domain of C21orf2 in Japanese patients with retinitis pigmentosa and cone-rod dystrophy. *Invest Ophthalmol Vis Sci* 57:4255–4263. <https://doi.org/10.1167/iovs.16-19450>
29. Khan AO, Eisenberger T, Nagel-Wolfrum K, Wolfrum U, Bolz HJ (2015) C21orf2 is mutated in recessive early-onset retinal dystrophy with macular staphyloma and encodes a protein that localises to the photoreceptor primary cilium. *Br J Ophthalmol* 99:1725–1731. <https://doi.org/10.1136/bjophthalmol-2015-307277>
30. McInerney-Leo AM, Wheeler L, Marshall MS, Anderson LK, Zankl A, Brown MA, Leo PJ, Wicking C, Duncan EL (2017) Homozygous variant in C21orf2 in a case of Jeune syndrome with severe thoracic involvement: extending the phenotypic spectrum. *Am J Med Genet A* 173:1698–1704. <https://doi.org/10.1002/ajmg.a.38215>
31. Wang Z, Iida A, Miyake N, Nishiguchi KM, Fujita K, Nakazawa T, Alswaid A, Albalwi MA et al (2016) Axial spondylometaphyseal dysplasia is caused by C21orf2 mutations. *PLoS ONE* 11:e0150555. <https://doi.org/10.1371/journal.pone.0150555>
32. Scott HS, Kyriakou DS, Peterson P, Heino M, Tähtinen M, Krohn K, Chen H, Rossier C, Lalioti MD, Antonarakis SE (1998) Characterization of a novel gene, C21orf2, on human chromosome 21q22.3 and its exclusion as the APECED gene by mutation analysis. *Genomics* 47:64–70. <https://doi.org/10.1006/geno.1997.5066>
33. Chen Y, Chen PL, Chen CF, Jiang X, Riley DJ (2008) Never-in-mitosis related kinase 1 functions in DNA damage response and checkpoint control. *Cell Cycle* 7:3194–3201. <https://doi.org/10.4161/cc.7.20.6815>
34. Pelegrini AL, Moura DJ, Brenner BL, Ledur PF, Maques GP, Henriques JAP, Saffi J, Lenz G (2010) Nek1 silencing slows down DNA repair and blocks DNA damage-induced cell cycle arrest. *Mutagenesis* 25:447–454. <https://doi.org/10.1093/mutage/geq026>
35. Liu S, Ho CK, Ouyang J, Zou L (2013) Nek1 kinase associates with ATR-ATRIP and primes ATR for efficient DNA damage signaling. *Proc Natl Acad Sci USA* 110(6):2175–2180. <https://doi.org/10.1073/pnas.1217781110>
36. Martins MB, Perez AM, Bohr VA, Wilson DM 3rd, Kobarg J (2021) NEK1 deficiency affects mitochondrial functions and the transcriptome of key DNA repair pathways. *Mutagenesis* 36(3):223–236. <https://doi.org/10.1093/mutage/geab011>
37. Singh V, Jaiswal PK, Ghosh I, Koul HK, Yu X, De Benedetti A (2019) Targeting the TLK1/NEK1 DDR axis with Thioridazine suppresses outgrowth of androgen independent prostate tumors. *Int J Cancer* 145:1055–1067. <https://doi.org/10.1002/ijc.32200>
38. Karle KN, Möckel D, Reid E, Schöls L (2012) Axonal transport deficit in a KIF5A (-/-) mouse model. *Neurogenetics* 13:169–179. <https://doi.org/10.1007/s10048-012-0324-y>
39. Campbell PD, Shen K, Sapio MR, Glenn TD, Talbot WS, Marlow FL (2014) Unique function of Kinesin Kif5A in localization of mitochondria in axons. *J Neurosci* 34:14717–14732. <https://doi.org/10.1523/jneurosci.2770-14.2014>
40. Weidberg H, Elazar Z (2011) TBK1 mediates crosstalk between the innate immune response and autophagy. *Sci Signal* 4:39. <https://doi.org/10.1126/scisignal.2002355>
41. Yu T, Yi YS, Yang Y, Oh J, Jeong D, Cho JY (2012) The pivotal role of TBK1 in inflammatory responses mediated by macrophages. *Mediators Inflamm* 2012:979105. <https://doi.org/10.1155/2012/979105>
42. Oakes JA, Davies MC, Collins MO (2017) TBK1: a new player in ALS linking autophagy and neuroinflammation. *Mol Brain* 10:1–10. <https://doi.org/10.1186/s13041-017-0287-x>
43. Goncalves A, Bürckstümmer T, Dixit E, Scheicher R, Górna MW, Karayel E, Sugar C, Stukalov A et al (2011) Functional dissection of the TBK1 molecular network. *PLoS ONE* 6:e23971. <https://doi.org/10.1371/journal.pone.0023971>
44. Moniz L, Dutt P, Haider N, Stambolic V (2011) Nek family of kinases in cell cycle, checkpoint control and cancer. *Cell Div* 6:18. <https://doi.org/10.1186/1747-1028-6-18>
45. Fry AM, O'Regan L, Sabir SR, Bayliss R (2012) Cell cycle regulation by the NEK family of protein kinases. *J Cell Sci* 125:4423–4433. <https://doi.org/10.1242/jcs.111195>
46. Mahjoub MR, Trapp ML, Quarmby LM (2005) NIMA-related kinases defective in murine models of polycystic kidney diseases localize to primary cilia and centrosomes. *J Am Soc Nephrol* 16(12):3485–3489. <https://doi.org/10.1681/asn.2005080824>
47. White MC, Quarmby LM (2008) The NIMA-family kinase, Nek1 affects the stability of centrosomes and ciliogenesis. *BMC Cell Biol* 9:29. <https://doi.org/10.1186/1471-2121-9-29>
48. Shalom O, Shalva N, Altschuler Y, Motro B (2008) The mammalian Nek1 kinase is involved in primary cilium formation. *FEBS Lett* 582:1465–1470. <https://doi.org/10.1016/j.febslet.2008.03.036>
49. Patil M, Pabla N, Huang S, Dong Z (2013) Nek1 phosphorylates Von Hippel-Lindau tumor suppressor to promote its proteasomal degradation and ciliary destabilization. *Cell Cycle* 12:166–171. <https://doi.org/10.4161/cc.23053>
50. Polci R, Peng A, Chen PL, Riley DJ, Chen Y (2004) NIMA-related protein kinase 1 is involved early in the ionizing radiation-induced DNA damage response. *Can Res* 64:8800–8803. <https://doi.org/10.1158/0008-5472.can-04-2243>
51. Watanabe Y, Nakagawa T, Akiyama T, Nakagawa M, Suzuki N, Warita H, Aoki M, Nakayama K (2020) An amyotrophic lateral sclerosis-associated mutant of C21ORF2 is stabilized by NEK1-mediated hyperphosphorylation and the inability to bind FBXO3. *iScience* 23:101491. <https://doi.org/10.1016/j.isci.2020.101491>
52. Gregorczyk M, Pastore G, Muñoz I, Carroll T, Streubel J, Munro M, Lis P, Lange S, Lamoliatte F, et al (2023) Functional characterization of C21ORF2 association with the NEK1 kinase mutated in human in diseases. *Life Sci Alliance* 6:202201740. <https://doi.org/10.26508/lsa.202201740>
53. Kapitein LC, Hoogenraad CC (2015) Building the neuronal microtubule cytoskeleton. *Neuron* 87:492–506. <https://doi.org/10.1016/j.neuron.2015.05.046>
54. Kallberg M, Wang H, Wang S, Peng J, Wang Z, Lu H, Xu J (2012) Template-based protein structure modeling using the RaptorX web server. *Nat Protoc* 7:1511–1522. <https://doi.org/10.1038/nprot.2012.085>
55. Iyer S, Acharya KR, Subramanian V (2019) Prediction of structural consequences for disease causing variants in C21orf2 protein using computational approaches. *J Biomol Struct Dyn* 37:465–480. <https://doi.org/10.1080/07391102.2018.1429313>
56. Santos DP, Kiskinis E, Eggan K, Merkle FT (2016) Comprehensive protocols for CRISPR/Cas9-based gene editing in human pluripotent stem cells. *Curr Protoc Stem Cell Biol*. 38:5B.6.1–5B.6.60. <https://doi.org/10.1002/cpsc.15>
57. Zaghloul NA, Katsanis N (2011) Zebrafish assays of ciliopathies. *Methods Cell Biol* 105:257–272. <https://doi.org/10.1016/b978-0-12-381320-6.00011-4>
58. Maerz LD, Casar Tena T, Gerhards J, Donow C, Jeggo PA, Philipp M (2019) Analysis of cilia dysfunction phenotypes in zebrafish embryos depleted of origin recognition complex factors. *Eur J Hum Genet* 27:772–782. <https://doi.org/10.1038/s41431-019-0338-0>
59. Shi Y, Su Y, Lipschutz JH, Lobo GP (2017) Zebrafish as models to study ciliopathies of the eye and kidney. *Clin Nephrol Res* 1:6–9
60. Shinbashi M, Jewell A, Randolph J, Couser N (2023) C21orf2 variants causing inherited retinal disease: a review of what we know and a report of two new suspected cases. *Clin Case Rep* 11:e7110. <https://doi.org/10.1002/ccr3.7110>

61. Sakowski SA, Lunn JS, Busta AS, Palmer M, Dowling JJ, Feldman EL (2012) A novel approach to study motor neurons from zebrafish embryos and larvae in culture. *J Neurosci Methods* 205:277–282. <https://doi.org/10.1016/j.jneumeth.2012.01.007>
62. Sakowski SA, Lunn JS, Busta AS, Oh SS, Zamora-Berridi G, Palmer M, Rosenberg AA, Philip SG, Dowling JJ, Feldman EL (2012) Neuromuscular effects of G93A-SOD1 expression in zebrafish. *Mol Neurodegener* 7:44. <https://doi.org/10.1186/1750-1326-7-44>
63. Singh J, Patten SA (2022) Modeling neuromuscular diseases in zebrafish. *Front Mol Neurosci* 15:1054573. <https://doi.org/10.3389/fnmol.2022.1054573>
64. Johnson JO, Mandrioli J, Benatar M, Abramzon Y, Van Deerlin VM, Trojanowski JQ, Gibbs JR et al (2010) Exome sequencing reveals VCP mutations as a cause of familial ALS. *Neuron* 68:857–864. <https://doi.org/10.1016/j.neuron.2010.11.036>
65. Nishimura AL, Mitne-Neto M, Silva HCA, Richieri-Costa A, Middleton S, Cascio D, Kok F, Oliveira JRM, Gillingwater T, Webb J, Skehel P, Zatz M (2004) A mutation in the vesicle-trafficking protein VAPB causes late-onset spinal muscular atrophy and amyotrophic lateral sclerosis. *Am J Hum Genet* 75:822–831. <https://doi.org/10.1086/425287>
66. Maruyama H, Morino H, Ito H, Izumi Y, Kato H, Watanabe Y, Kinoshita Y, Kamada M, Nodera H et al (2010) Mutations of optineurin in amyotrophic lateral sclerosis. *Nature* 465:223–226. <https://doi.org/10.1038/nature08971>
67. Deng HX, Chen W, Hong ST, Boycott KM, Gorrie GH, Siddique N, Yang Y, Fecto F, Shi Y, Zhai H et al (2011) Mutations in UBQLN2 cause dominant X-linked juvenile and adult-onset ALS and ALS/dementia. *Nature* 477:211–215. <https://doi.org/10.1038/nature10353>
68. Fecto F, Yan J, Vemula SP, Liu E, Yang Y, Chen W, Zheng JG, Shi Y, Siddique N, Arrat H, Donkervoort S et al (2011) SQSTM1 mutations in familial and sporadic amyotrophic lateral sclerosis. *Arch Neurol* 68(11):1440–1446. <https://doi.org/10.1001/archneurol.2011.250>
69. Farhan SMK, Howrigan DP, Abbott LE, Klim JR, Topp SD, Byrnes AE, Churchhouse C, Patnani H et al (2019) Exome sequencing in amyotrophic lateral sclerosis implicates a novel gene, DNAJC7, encoding a heat-shock protein. *Nat Neurosci* 22:1966–1974. <https://doi.org/10.1038/s41593-019-0530-0>
70. Kalmar B, Greensmith L (2017) Cellular chaperones as therapeutic targets in ALS to restore protein homeostasis and improve cellular function. *Front Mol Neurosci* 10:251. <https://doi.org/10.3389/fnmol.2017.00251>
71. Wright GSA (2020) Molecular and pharmacological chaperones for SOD1. *Biochem Soc Transact* 48:1795–1806. <https://doi.org/10.1042/bst20200318>
72. Neumann M, Sampathu DM, Kwong LK, Truax AC, Micsenyi MC, Chou TT, Bruce J, Schuck T et al (2006) Ubiquitinated TDP-43 in frontotemporal lobar degeneration and amyotrophic lateral sclerosis. *Science* 314:130–133. <https://doi.org/10.1126/science.1134108>
73. Shibata N, Asayama K, Hirano A, Kobayashi M (1996) Immunohistochemical study on superoxide dismutases in spinal cords from autopsied patients with amyotrophic lateral sclerosis. *Dev Neurosci* 18:492–498. <https://doi.org/10.1159/00011445>
74. Kwiatkowski TJ Jr, Bosco DA, Leclerc AL, Tamrazian E, Vanderburg CR, Russ C, Davis A, Gilchrist J et al (2009) Mutations in the FUS/TLS gene on chromosome 16 cause familial amyotrophic lateral sclerosis. *Science* 323:1205–1208. <https://doi.org/10.1126/science.1166066>
75. Vance C, Rogelj B, Hortobágyi T, De Vos KJ, Nishimura AL, Sreedharan J, Hu X, Smith B et al (2009) Mutations in FUS, an RNA processing protein, cause familial amyotrophic lateral sclerosis type 6. *Science* 323:1208–1211. <https://doi.org/10.1126/science.1165942>
76. Ash PE, Bieniek KF, Gendron TF, Caulfield T, Lin WL, DeJesus-Hernandez M et al (2013) Unconventional translation of C9ORF72 GGGGCC expansion generates insoluble polypeptides specific to c9FTD/ALS. *Neuron* 77:639–646. <https://doi.org/10.1016/j.neuron.2013.02.004>
77. Gendron TF, Bieniek KF, Zhang YJ, Jansen-West K, Ash PE, Caulfield T, Daugherty L, Dunmore JH (2013) Antisense transcripts of the expanded C9ORF72 hexanucleotide repeat form nuclear RNA foci and undergo repeat-associated non-ATG translation in c9FTD/ALS. *Acta Neuropathol* 126:829–844. <https://doi.org/10.1007/s00401-013-1192-8>
78. Mori K, Arzberger T, Grässer FA, Gijssels I, May S, Rentzsch K, Weng SM, Schludi MH et al (2013) Bidirectional transcripts of the expanded C9orf72 hexanucleotide repeat are translated into aggregating dipeptide repeat proteins. *Acta Neuropathol* 126:881–893. <https://doi.org/10.1007/s00401-013-1189-3>
79. Pair FS, Yacoubian TA (2021) 14–3–3 Proteins: novel pharmacological targets in neurodegenerative diseases. *Trends Pharmacol Sci* 42:226–238. <https://doi.org/10.1016/j.tips.2021.01.001>
80. Umahara T, Uchiyama T, Shibata N, Nakamura A, Hanyu H (2016) 14–3–3 eta isoform colocalizes TDP-43 on the coarse granules in the anterior horn cells of patients with sporadic amyotrophic lateral sclerosis. *Brain Res* 1646:132–138. <https://doi.org/10.1016/j.brainres.2016.05.051>
81. Park JH, Jang HR, Lee IY, Oh HK, Choi EJ, Rhim H, Kang S (2017) Amyotrophic lateral sclerosis-related mutant superoxide dismutase 1 aggregates inhibit 14–3–3-mediated cell survival by sequestration into the JUNQ compartment. *Hum Mol Genet* 26:3615–3629. <https://doi.org/10.1093/hmg/ddx250>
82. Ke YD, van Hummel A, Au C, Chan G, Lee WS, van der Hoven J, Przybyla M, Deng Y, Sabale M et al (2024) Targeting 14–3–3-mediated TDP-43 pathology in amyotrophic lateral sclerosis and frontotemporal dementia mice. *Neuron* S0896–6273:00048–00055. <https://doi.org/10.1016/j.neuron.2024.01.022>
83. van Rheenen W, van der Spek RAA, Bakker MK, van Vugt JJFA, Hop PJ, Zwamborn RAJ et al (2021) Common and rare variant association analyses in amyotrophic lateral sclerosis identify 15 risk loci with distinct genetic architectures and neuron-specific biology. *Nat Genet* 53:1636–1648. <https://doi.org/10.1038/s41588-021-00973-1>
84. Matsushima N, Miyashita H, Kretsinger RH (2021) Sequence features, structure, ligand interaction, and diseases in small leucine rich repeat proteoglycans. *J Cell Commun Signal* 15:519–531. <https://doi.org/10.1007/s12079-021-00616-4>
85. Martínez-Silva ML, Imhoff-Manuel RD, Sharma A, Heckman CJ, Shneider NA, Roselli F, Zytznick D, Manuel M (2018) Hypoexcitability precedes denervation in the large fast-contracting motor units in two unrelated mouse models of ALS. *Elife* 7:e30955. <https://doi.org/10.7554/elife.30955>
86. Huang X, Roet KCD, Zhang L, Brault A, Berg AP, Jefferson AB, Klug-McLeod J, Leach KL et al (2021) Human amyotrophic lateral sclerosis excitability phenotype screen: target discovery and validation. *Cell Rep* 35:109224. <https://doi.org/10.1016/j.celrep.2021.109224>
87. Sommer D, Rajkumar S, Seidel M, Aly A, Ludolph A, Ho R, Boeckers TM, Catanese A (2022) Aging-dependent altered transcriptional programs underlie activity impairments in human C9orf72-mutant motor neurons. *Front Mol Neurosci* 15:894230. <https://doi.org/10.3389/fnmol.2022.894230>
88. Krohn K, Ovod V, Vilja P, Heino M, Scott H, Kyriakou DS, Antonarakis S, Jacobs HT, Isola J, Peterson P (1997) Immunohistochemical characterization of a novel mitochondrially located protein encoded by a nuclear gene within the DFNB8/10 critical region on 21q22.3. *Biochem Biophys Res Commun* 238:806–810. <https://doi.org/10.1006/bbrc.1997.7352>
89. Walz G (2017) Role of primary cilia in non-dividing and post-mitotic cells. *Cell Tissue Res* 369:11–25. <https://doi.org/10.1007/s00441-017-2599-7>
90. Morrison CG (2021) Primary cilia and the DNA damage response: linking a cellular antenna and nuclear signals. *Biochem Soc Trans* 49:829–841. <https://doi.org/10.1042/bst20200751>
91. DeDecker M, Zelina P, Moens GT, Eggemont K, Moisse M, Veldink JH, Van Den Bosch L, Pasterkamp RJ, Van Damme P (2022) C21orf2 mutations found in ALS disrupt primary cilia function. <https://doi.org/10.1101/2022.02.28.482239>.
92. Melo-Hanchuk TD, Slepicka PF, Meirelles GV, Basei FL, Lovato DV, Granato DC, Pauletti BA et al (2017) NEK1 kinase domain structure and its dynamic protein interactome after exposure to Cisplatin. *Sci Rep* 7:5445. <https://doi.org/10.1038/s41598-017-05325-w>
93. Chen Y, Craigen WJ, Riley DJ (2009) Nek1 regulates cell death and mitochondrial membrane permeability through phosphorylation of VDAC1. *Cell Cycle* 8:257–267. <https://doi.org/10.4161/cc.8.2.7551>
94. Chen Y, Gaczynska M, Osmulski P, Polci R, Riley DJ (2010) Phosphorylation by Nek1 regulates opening and closing of voltage dependent anion channel 1. *Biochem Biophys Res Commun* 394:798–803. <https://doi.org/10.1016/j.bbrc.2010.03.077>
95. Higelin J, Catanese A, Semelink-Sedlacek LL, Oetzuerk S, Lutz AK, Bausinger J, Barbi G, Speit G et al (2018) NEK1 loss-of-function mutation

- induces DNA damage accumulation in ALS patient-derived motoneurons. *Stem Cell Res* 30:150–162. <https://doi.org/10.1016/j.scr.2018.06.005>
96. Singh V, Khalil MI, De Benedetti A (2020) The TLK1/Nek1 axis contributes to mitochondrial integrity and apoptosis prevention via phosphorylation of VDAC1. *Cell Cycle* 19:363–375. <https://doi.org/10.1080/15384101.2019.1711317>
 97. Du ZW, Chen H, Liu H, Lu J, Qian K, Huang CL, Zhong X, Fan F, Zhang SC (2015) Generation and expansion of highly pure motor neuron progenitors from human pluripotent stem cells. *Nat Commun* 6:6626. <https://doi.org/10.1038/ncomms7626>
 98. Perez-Riverol Y, Bai J, Bandla C, Hewapathirana S, García-Seisdedos D, Kamatchinathan S, Kundu D et al (2022) The PRIDE database resources in 2022: a Hub for mass spectrometry-based proteomics evidences. *Nucleic Acids Res* 50(D1):D543–D552. <https://doi.org/10.1093/nar/gkab1038>
 99. Deutsch EW, Bandeira N, Perez-Riverol Y, Sharma V, Carver J, Mendoza L, Kundu DJ, Wang S et al (2023) The proteomexchange consortium at 10 years: 2023 update. *Nucleic Acids Res* 51(D1):D1539–D1548. <https://doi.org/10.1093/nar/gkac1040>
 100. Heberle H, Meirelles GV, da Silva FR, Telles GP, Minghim R (2015) InteractiVenn: a web-based tool for the analysis of sets through Venn diagrams. *BMC Bioinform* 16:169. <https://doi.org/10.1186/s12859-015-0611-3>
 101. D'Astolfo DS, Pagliero RJ, Pras A, Karthaus WR, Clevers H, Prasad V, Lebbink RJ, Rehmann H, Geijsen N (2015) Efficient intracellular delivery of native proteins. *Cell* 161:674–690. <https://doi.org/10.1016/j.cell.2015.03.028>
 102. Divakaruni AS, Paradise A, Ferrick DA, Murphy AN, Jastroch M (2014) Analysis and interpretation of microplate-based oxygen consumption and pH data. *Methods Enzymol* 547:309–354. <https://doi.org/10.1016/b978-0-12-801415-8.00016-3>
 103. Westerfield M (1993) *The Zebrafish Book: A Guide for the Laboratory use of Zebrafish (Brachydanio rerio)*. University of Oregon Press

Publisher's Note

Springer Nature remains neutral with regard to jurisdictional claims in published maps and institutional affiliations.